# Cell binding tropism of rat hepatitis E virus is a pivotal determinant of its zoonotic transmission to humans

Hongbo Guo[a,1,2], Jiaqi Xu[a,1], Jianwen Situ[b,1], Chunyang Li[a], Xia Wang[c], Yao Hou[a], Guangde Yang[c], Lingli Wang[a], Dong Ying[d], Zheng Li[a], Zijie Wang[a], Jia Su[e,f], Yibo Ding[a] [ID], Dou Zeng[a], Jikai Zhang[a], Xiaohui Ding[a], Shusheng Wu[b], Weiwei Miao[b], Renxian Tang[a] [ID], Yihan Lu[g], Huihui Kong[h] [ID], Peng Zhou[f] [ID], Zizheng Zheng[d], Kuiyang Zheng[a,2] [ID], Xiucheng Pan[c,2], Siddharth Sridhar[b,2], and Wenshi Wang[a,2] [ID]

Affiliations are included on p. 11.

Classically, all hepatitis E virus (HEV) variants causing human infection belong to the genus *Paslahepevirus* (HEV-A). However, the increasing cases of rat HEV infection in humans since 2018 challenged this dogma, posing increasing health threats. Herein, we investigated the underlying mechanisms dictating the zoonotic potentials of different HEV species and their possible cross-protection relationships. We found that rat HEV virus-like particles (HEV^VLPs) bound to human liver and intestinal cells/tissues with high efficiency. Moreover, rat HEV^VLPs and infectious rat HEV particles penetrated the cell membrane and entered human target cells postbinding. In contrast, ferret HEV^VLPs showed marginal cell binding and entry ability, bat HEV^VLPs and avian HEV^VLPs exhibited no binding and entry potency. Structure-based three-dimensional mapping identified that the surface spike domain of rat HEV is crucial for cell binding. Antigenic cartography indicated that rat HEV exhibited partial cross-reaction with HEV-A. Intriguingly, sera of HEV-A infected patients or human HEV vaccine Hecolin® immunized individuals provided partial cross-protection against the binding of rat HEV^VLPs to human target cells. In summary, the interactions between the viral capsid and cellular receptor(s) regulate the distinct zoonotic potentials of different HEV species. The systematic characterization of antigenic cartography and serological cross-reactivity of different HEV species provide valuable insights for the development of species-specific diagnosis and protective vaccines against zoonotic HEV infection.

hepatitis E virus | zoonosis | cell binding tropism | virus entry

Hepatitis E virus (HEV) is the most common cause of viral hepatitis worldwide, with estimated 20 million infections and around 60,000 fatalities annually. In resource-limited settings (e.g., among refugees and internally displaced groups), hepatitis E outbreaks periodically occur, presenting significant humanitarian emergencies (1). In developed countries, HEV commonly causes zoonotic food-borne infections. HEV infection can be aggravated in pregnant women, and patients with preexisting liver disease, resulting in severe complications and high mortality rate (up to 45% in some endemic regions with HEV-1 and -2) in recorded outbreaks (1).

Distinct from all the other human hepatitis viruses, HEV is the only one that is zoonotic (2). HEV belongs to the *Hepeviridae* family divided into two subfamilies: *Orthohepevirinae* and *Parahepevirinae*. *Orthohepevirinae* includes four genera that are phylogenetically distinct and have different host ranges (3). They are classified as *Paslahepevirus* (referred to as HEV-A; including eight genotypes HEV-1 to HEV-8; isolates from humans, swine, deer, mongoose, rabbit, and camel), *Avihepevirus* (referred to as HEV-B; isolates from avian), *Rocahepevirus* (referred to as HEV-C; isolates from rat, greater bandicoot, Asian musk shrew, ferret and mink), and *Chirohepevirus* (referred to as HEV-D; isolates from bat) (4). Classically, human diseases are thought to be exclusively caused by *Paslahepevirus*, which include both zoonotic (e.g., HEV-3 and 4) and nonzoonotic (e.g., HEV-1 and 2) strains. However, increasing cases of hepatitis E have been reported to be associated with the infection of rat HEV in multiple regions since 2018 (5–12), and recently, two children with acute hepatitis of unknown origin were found to have rat hepatitis E virus infection in Spain (13). This indicates that rat HEV, which is classified as HEV-C1 clade of *Rocahepevirus*, can cross species barrier to cause zoonotic infection in humans (5, 6, 12). In contrast, no *Avihepevirus* or *Chirohepevirus*-related human infections have been reported to date. The zoonotic potential of these genetically distinct HEV species has raised great public health concerns. It seems that different HEV species have differential potential of zoonotic transmission, but the underlying mechanisms remain unknown.

## Significance

Classically, all hepatitis E virus (HEV) variants causing human infection belong to HEV-A. However, the increasing cases of rat HEV infection in humans challenged this dogma. We found that cell binding tropism is a pivotal determinant of HEV species regarding their zoonotic transmission to humans. Rat HEV virus-like particles (VLPs) and infectious rat HEV bind and enter human target cells, whereas ferret, bat and avian HEV VLPs show marginal or no cell binding and entry potency. Rat HEV exhibited partial cross-reaction with HEV-A, and anti-HEV-A sera partially cross-inhibited the binding of rat HEV^VLPs to human target cells. Our study revealed mechanistic insights regarding the distinct zoonotic potential of different HEV species and elucidated their cross-species antigenic relationships and serological responses.

[1]H.G., J.X., and J.S. contributed equally to this work.

[2]To whom correspondence may be addressed. Email: Hongbo.guo@xzhmu.edu.cn, zky@xzhmu.edu.cn, xzpxc68@126.com, sid8998@hku.hk, or wenshi.wang@xzhmu.edu.cn.

Viral entry is the first determinant of host tropism and the ability of cross-species transmission. This step is initiated by specific binding of virions to the receptor(s) on the cell membrane (14, 15). There are two forms of HEV particles in the infected host. In general, the naked, nonenveloped virions (nHEV) are shed into feces to mediate interhost transmission, whereas quasienveloped virions (eHEV) circulate in blood to spread the virus within the host (16). nHEV compared to eHEV has a 10-fold higher infectivity due to a higher efficiency in cell attachment (16, 17). Interestingly, it has been recently reported that nHEV can also be detected in plasma of infected patients, suggesting that nHEV may mediate both interhost and intrahost spreading (18). We postulate that the entry of nHEV through direct interactions between the viral capsid and cellular receptor(s) is one of the key determinants of host tropism and zoonotic transmission.

In this study, we aim to understand the underlying mechanisms dictating the distinct zoonotic potentials of different HEV species. HEV grows poorly in cell culture (19, 20). Here, we took the advantage that the HEV capsid protein ORF2 can assemble into virus-like particles (VLPs) in vitro (21–23). These VLPs are believed to mimic live viruses in binding and penetrating host cells, constituting a good model for studying viral entry (24, 25). Thus, we generated VLPs for all HEV species and comparatively assessed their host tropism in multiple cell lines and human liver and intestinal tissue slides. Strikingly, rat HEV (HEV-C1) VLPs bind to human liver and intestinal cells/tissues with high efficiency and specificity. Moreover, HEV-C1$^{VLPs}$ penetrate the cell membrane and enter target cells postbinding. This observation was further confirmed by employing infectious rat HEV particles. In contrast, ferret HEV$^{VLPs}$ showed marginal cell binding and entry ability, bat HEV$^{VLPs}$ and avian HEV$^{VLPs}$ exhibited no cell binding and entry. Antigenic cartography indicated that rat HEV exhibited partial cross-reaction with HEV-A. More intriguingly, HEV-A$^{VLP}$ immunized rat sera, HEV-A infected patient sera, and human HEV vaccine Hecolin® immunized individual sera partially cross-inhibited the binding of HEV-C1$^{VLP}$ to human target cells. These findings revealed mechanistic insights regarding the distinct zoonotic potential of different HEV species and elucidated their cross-species antigenic relationships and serological responses.

## Results

### The Capsid ORF2 Proteins (a.a.368 to 606) of All HEV Species Self-Assemble into VLPs and Exhibit Specific Binding Affinity to Their Cognate Liver Tissues.

Phylogenetic analysis of different HEV species was performed based on ORF2 amino acid sequences of the reference HEV sequences (Fig. 1*A* and *SI Appendix*, Fig. S1) (3, 26, 27). The sequence identity of ORF2 is relatively low (~50%) among different HEV species (*SI Appendix*, Table S1). However, ORF2 is highly conserved within species. Specifically, the identity of HEV-A (refer to *Paslahepevirus*) ORF2 ≥ 90%, HEV-B (refer to *Avihepevirus*) ORF2 ≥ 90%, HEV-C1 (refer to *Rocahepevirus*, rat HEV) ORF2 ≥ 91%, HEV-C2 (refer to *Rocahepevirus*, ferret HEV) ORF2 ≥ 98%, and HEV-D (refer to *Chirohepevirus*) ORF2 ≥ 80% (Datasets S1–S5). The ORF2 consensus sequences were used to represent different variants within each species (*SI Appendix*, Fig. S2 and Table S2).

For HEV-A strains (e.g., HEV-1), the ORF2 region spanning from a.a.368 to 606 can self-assemble into VLPs (*SI Appendix*, Fig. S3) (22). Hence, the corresponding regions of ORF2 of each species were expressed and named HEV-A ORF2$^T$, HEV-B ORF2$^T$, HEV-C1 ORF2$^T$, HEV-C2 ORF2$^T$, and HEV-D ORF2$^T$, respectively (*SI Appendix*, Fig. S2). The formation of dimers and multimers is a key step of VLP assembly (21). Indeed,

dimers (40 to 55 kDa) and multimers (including pentamers ~180 kDa) were successfully detected, then resolved into ~35 kDa monomers upon boiling treatment (Fig. 1 *B*, *E*, *H*, *K*, and *N* and *SI Appendix*, Fig. S4 *A*, *B*, *D*, *E*, *G*, *H*, *J*, *K*, *M*, and *N*). Electron microscopy analysis confirmed the successful assembly of VLPs of all HEV species (Fig. 1 *C*, *F*, *I*, *L*, and *O*). Accordingly, we named the VLPs HEV-A$^{VLP}$, HEV-B$^{VLP}$, HEV-C1$^{VLP}$, HEV-C2$^{VLP}$, and HEV-D$^{VLP}$, respectively. To validate whether these VLPs could authentically mimic cell binding of infectious virus particles, liver tissue slides from five different host species (human, chicken, rat, ferret, and bat) were collected. All five VLPs could efficiently bind to the liver tissue slides of their cognate host, while denatured VLPs lost their binding ability (*SI Appendix*, Fig. S4 *C*, *F*, *I*, *L*, and *O*). These results indicated that the structure and conformation of VLPs were essential for binding to their target cells. Moreover, the binding of VLPs to their cognate liver cells was blocked by rat sera immunized with their corresponding VLPs, but not the negative control sera (Fig. 1 *D*, *G*, *J*, *M*, and *P*). These data demonstrate that the VLPs of five HEV species accurately mimic cell-binding of infectious virus particles and exhibit specific binding to their cognate liver tissues.

### HEV-C1$^{VLP}$ Efficiently Binds to Human-Derived Intestinal and Liver Cells/Tissues with High Specificity.

Five VLPs possess specific cell-binding abilities, suitable for studying cell-binding tropism. Hence, VLPs of different HEV species were subjected to cell binding assays with human liver and intestinal cell lines. HEV-1$^{VLP}$, the main component of human HEV vaccine Hecolin® (28) served as a positive control (*SI Appendix*, Fig. S5). HEV-1$^{VLP}$ efficiently bound to HepG2, HuH7, and Caco2 cells. Rat sera immunized with HEV-A$^{VLP}$, but not the negative control sera, abrogated the binding of HEV-1$^{VLP}$, highlighting the specificity of this assay (*SI Appendix*, Fig. S5). Notably, HEV-C2$^{VLP}$ showed marginal binding to HepG2, HuH7, and Caco2 cells, and HEV-B$^{VLP}$ and HEV-D$^{VLP}$ exhibited no binding affinity (Fig. 2*A*). Conversely, although the sequence identity is relatively low (~50%) between HEV-A ORF2 and HEV-C1 ORF2 (*SI Appendix*, Tables S1 and S2), HEV-C1$^{VLP}$ exhibited high binding affinity to human liver and intestinal cell lines (Fig. 2*A*, column 3 and Fig. 2*B*). Interestingly, similar binding tropism was also observed in rat liver cells RH-35 (Fig. 2 *A* and *B*). Moreover, HEV-C1$^{VLP}$ efficiently bound to human liver and intestinal tissue slides (Fig. 2 *C* and *D*). Anti-HEV-C1$^{VLP}$ sera, but not the negative control sera, inhibited the binding of HEV-C1$^{VLP}$ to human liver and intestinal tissues. These results implied that HEV-C1$^{VLP}$ may utilize the same binding sites (liver and intestine) as HEV-A to cause infection. In summary, among different HEV species, HEV-C1$^{VLP}$ efficiently binds to human-derived target cells and tissues.

### HEV-C1$^{VLP}$ and Rat HEV Complete the Entry Step and Migrate into Human Target Cells.

Upon specific binding to the receptor(s), virions need to penetrate the cell membrane and enter the target cells to complete the so-called virus entry process. Herein, we inoculated HepG2 and RH-35 cells with the same amounts of VLPs. Consistent with their binding tropism, we detected marginal signal of HEV-C2$^{VLP}$ within HepG2 and RH-35 cells, and no HEV-B$^{VLP}$ and HEV-D$^{VLP}$ signals (Fig. 3 *A–C*). Nevertheless, significant amounts of HEV-C1$^{VLP}$ and HEV-A$^{VLP}$ were observed within HepG2 and RH-35 cells (Fig. 3 *A–C*, column 1 and 3). Furthermore, in parallel with the entry of human HEV-3 in HepG2 cells, rat HEV entered HepG2 and RH-35 cells (*SI Appendix*, Fig. S6 *A–C*). More convincingly, both RT-qPCR and immunofluorescent analysis indicated that the entry of rat HEV into HepG2 and RH-35 cells was significantly inhibited
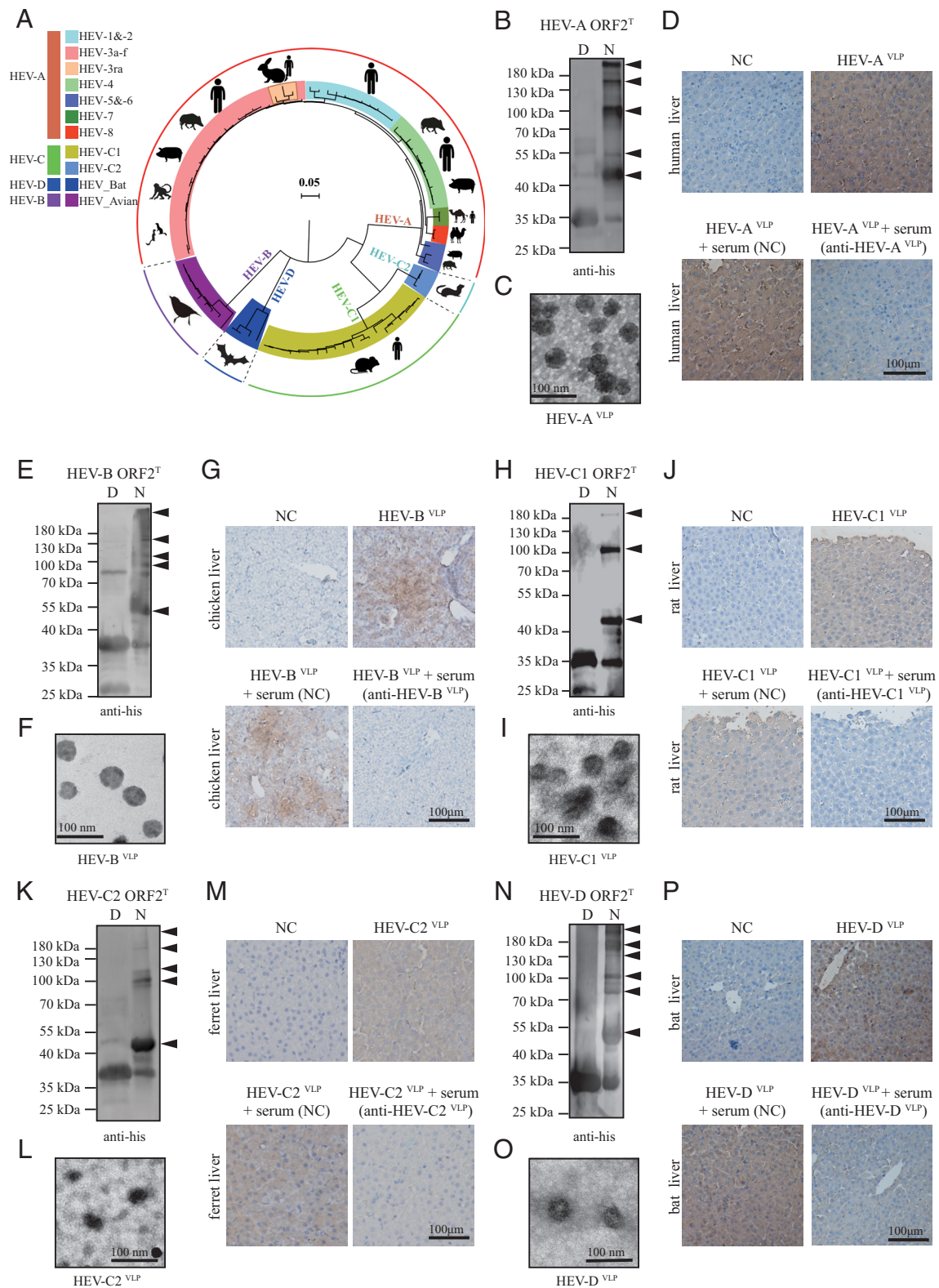
**Fig. 1.** Generation and characterization of VLPs of HEV A-D. (*A*) The Neighbor-Joining tree was constructed based on the amino acid sequences of ORF2 protein of the reference HEV sequences (26, 27). The scale bar indicated the distances of ORF2 amino acid sequences. The colors on the branches indicate HEV genotypes. The colors of the outermost ring indicate HEV genera (A-D). Silhouettes represent the different hosts. (*B*) C-terminally his-tagged HEV-A ORF2$^T$ was expressed in *E. coli* and purified. Nondenatured (N) and denatured (D) HEV-A ORF2$^T$ proteins were analyzed by western blots with anti-his antibody. The dimer and multimeric proteins were indicated with black arrows. (*C*) Electron microscopic images of the self-assembled VLPs, named HEV-A$^{VLP}$. (*D*) Human liver tissue slides were incubated with PBS (NC), HEV-A$^{VLP}$, HEV-A$^{VLP}$ + NC serum (1:20), HEV-A$^{VLP}$ + anti-HEV-A$^{VLP}$ (1:20) overnight at 4 °C. The binding of HEV-A$^{VLP}$ to human liver tissue slides was detected by immunohistochemistry. (*E*–*G*) Same as (*B*–*D*) for the generation and characterization of HEV-B ORF2$^T$ and HEV-B$^{VLP}$. (*H*–*J*) Same as (*B*–*D*) for the generation and characterization of HEV-C1 ORF2$^T$ and HEV-C1$^{VLP}$. (*K*–*M*) Same as (*B*–*D*) for the generation and characterization of HEV-C2 ORF2$^T$ and HEV-C2$^{VLP}$. (*N*–*P*) Same as (*B*–*D*) for the generation and characterization of HEV-D ORF2$^T$ and HEV-D$^{VLP}$. The images presented are the representative of three independent experiments.
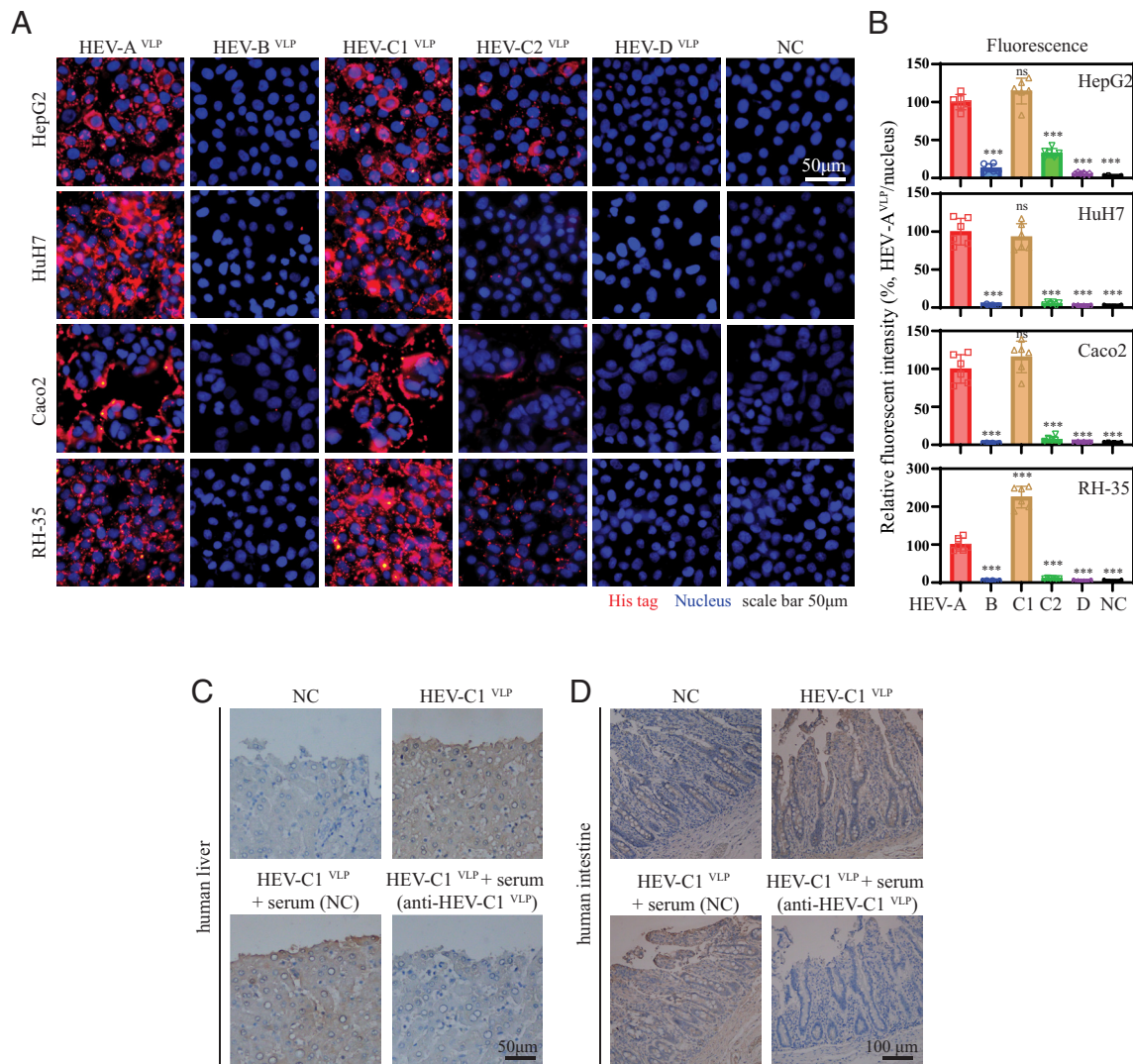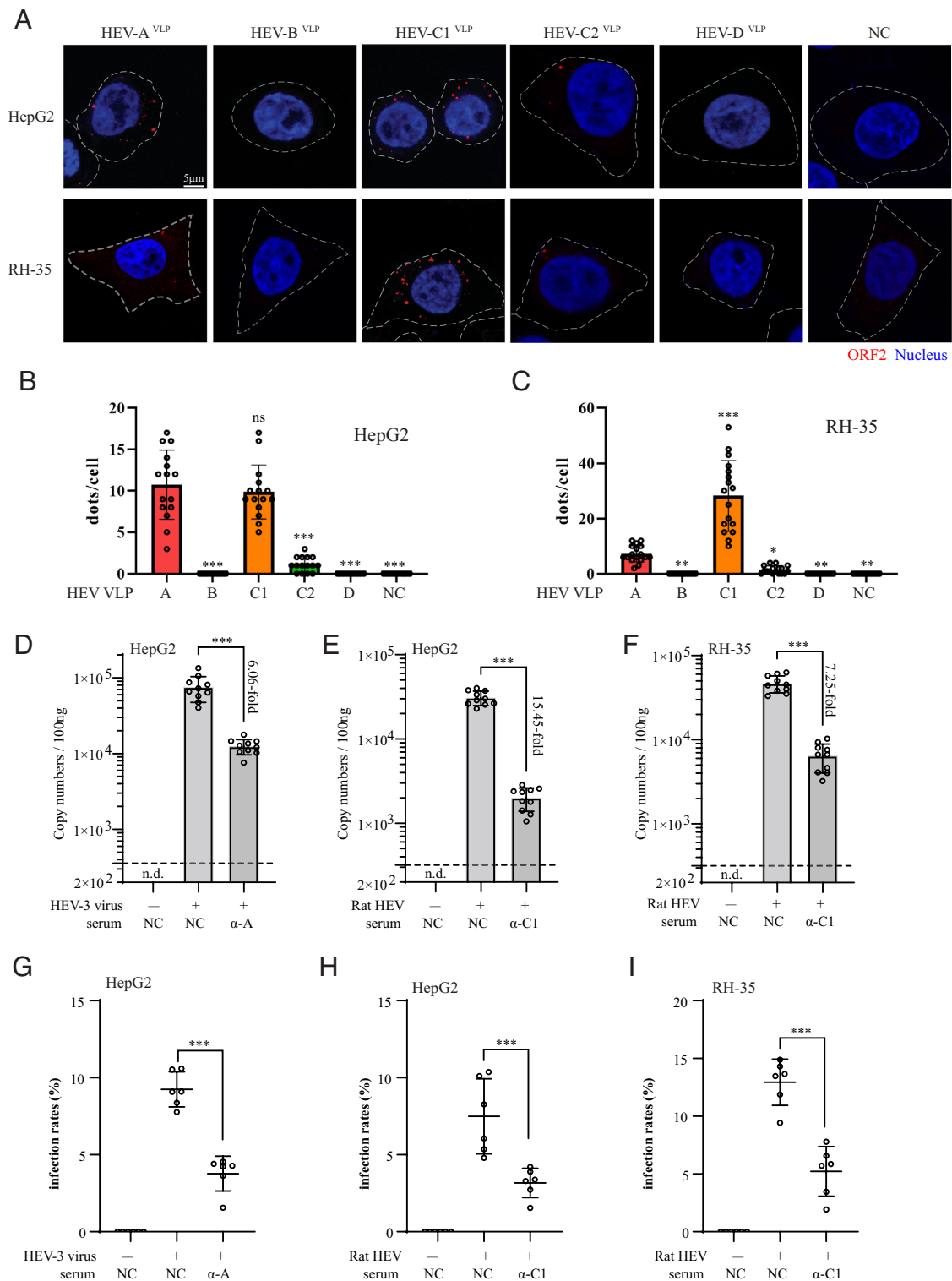
**Fig. 2.** Characterization of cell-binding capability of HEV A-D VLPs. (*A*) The binding capability of HEV-A$^{VLP}$, HEV-B$^{VLP}$, HEV-C1$^{VLP}$, HEV-C2$^{VLP}$, and HEV-D$^{VLP}$ to human liver cell lines (HepG2 and HuH7), human intestinal cell line (Caco2), and rat live cell line (RH-35) was measured by immunofluorescence assay. (*B*) The relative fluorescent intensity was quantified by ImageJ. The fluorescent intensity of HEV-A VLP was set as 100. The significance of difference between HEV-A$^{VLP}$ and the other groups was calculated based on three independent experiments. (*C*) Human liver tissue slides were incubated with PBS (NC), HEV-C1$^{VLP}$, HEV-C1$^{VLP}$ + NC serum (1:20), HEV-C1$^{VLP}$ + anti-HEV-C1$^{VLP}$ (1:20) overnight at 4 °C. The binding capacity of HEV-C1$^{VLP}$ was detected by immunohistochemistry. (*D*) Same as (*C*) for testing the binding of HEV-C1$^{VLP}$ to human intestinal tissue slides. The images presented are representative of three independent experiments.

by anti-HEV-C1$^{VLP}$ serum (Fig. 3 *D–I* and *SI Appendix*, Fig. S6 *D–F*). Collectively, these results demonstrated that HEV-C1$^{VLP}$ and infectious rat HEV particles possess the capability to enter human target cells.

**The Surface Spike Domain of Virion Capsid Dictates the Binding of HEV-C1.** The crucial cell binding sites on the ORF2 capsid of HEV-3 have been identified through VLP mutagenesis analysis (21). Three HEV-A$^{VLP}$ mutants were created by mutating key amino acid residues essential for binding to susceptible human cells (*SI Appendix*, Fig. S7 *A* and *B*). All three mutants can form multimers and self-assemble into VLPs (*SI Appendix*, Fig. S7 *C–H*). The wild-type (WT) HEV-A$^{VLP}$ could efficiently bind to the cellular membrane of HuH7, HepG2, Caco2, and RH-35 cells with high specificity (*SI Appendix*, Fig. S8). However, all three mutants lost their cell-binding capacity (*SI Appendix*, Fig. S8). These results confirmed that the produced VLPs served as a reliable toolset to identify the key regions of ORF2 that mediate the binding activity.

Consequently, 24 HEV-C1 ORF2$^T$ mutants were created based on 3D structure analysis (23) (Fig. 4*A*). For all mutants, 1 or 2
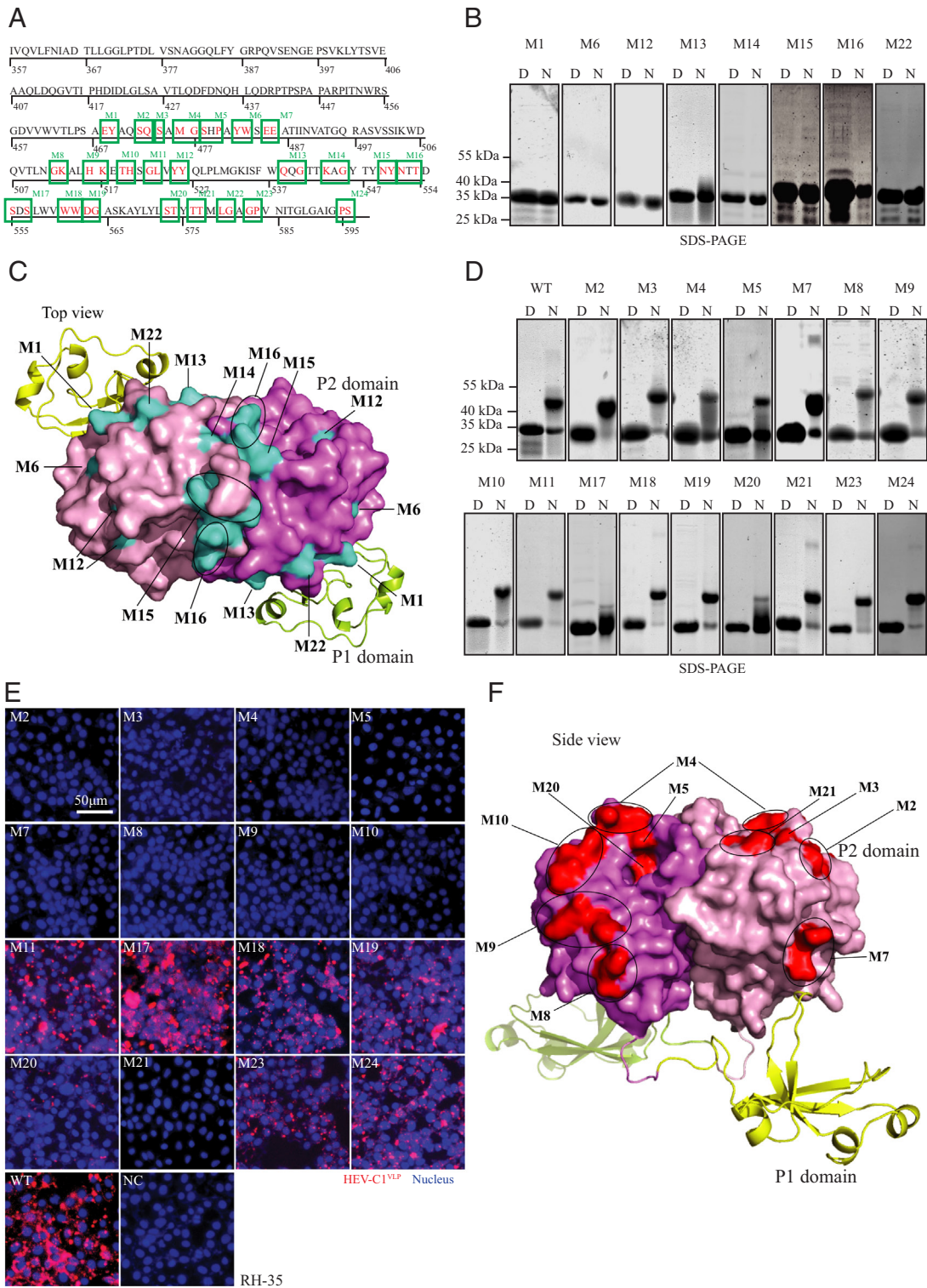
amino acid residues at the surface of the P domain were mutated to Alanine. Notably, eight mutants (M1, M6, M12, M13, M14, M15, M16, and M22) failed to form dimers, multimers, or self-assemble into VLPs (Fig. 4*B* and *SI Appendix*, Fig. S9). These results indicated that these residues are essential for HEV-C1 VLP formation (Fig. 4*C* and *SI Appendix*, Fig. S10). The remaining 16 mutants were able to form dimers, multimers, and self-assemble into VLPs (Fig. 4*D* and *SI Appendix*, Figs. S11 and S12). Their cell-binding ability to RH-35 cells was tested. Notably, nine mutants (M2, M3, M4, M5, M7, M8, M9, M10, and M21) lost their cell-binding competence, one mutant (M20) showed weak binding, and the remaining 6 mutants (M11, M17, M18, M19, M23, and M24) retained most of their binding capacity (Fig. 4*E*). Similar results were observed in HepG2 cells (*SI Appendix*, Fig. S13), indicating that the key regions responsible for binding to rat and human target cells are probably similar. These key residues were mapped on the 3D structure of ORF2. The conformational changes of each mutant were analyzed (Fig. 4*F* and *SI Appendix*, Figs. S14 and S15). Specifically, these residues are dispersed on the apical surface as well as the horizontal region of the spike domain (Fig. 4*F*). In summary, structure-based 3D

**Fig. 3.** Characterization of cell entry capability of HEV-C1$^{VLP}$ and rat HEV. (*A*) HepG2 and RH-35 cells were inoculated with the same amounts of VLPs. The entry of HEV-A$^{VLP}$, HEV-B$^{VLP}$, HEV-C1$^{VLP}$, HEV-C2$^{VLP}$, and HEV-D$^{VLP}$ to HepG2 and RH-35 cells was detected by confocal immunofluorescence assay. Bright-field microscopy channel was used to determine outlines of adherent cells. Cell boundary was illustrated with white dashed lines. (*B* and *C*) The intracellular positive fluorescent dots of five HEV VLPs were quantified based on three independent experiments. (*D*) HepG2 cells were inoculated with mock or human HEV-3 virus (~3.3 × 10$^3$ copy/cell) with rat NC serum (1:20), or anti-HEV-A$^{VLP}$ serum (1:20) overnight. The levels of intracellular HEV-3 RNA were quantified by RT-qPCR assay based on three independent experiments. n.d., not detected. (*E*) Same as (*D*), RT-qPCR detection of intracellular levels of rat HEV RNA in HepG2 cells post rat HEV (~1.3 × 10$^3$ copy/cell) inoculation. (*F*) Same as (*E*) for the detection of intracellular rat HEV RNA in RH-35 cells by RT-qPCR. (*G–I*) Same as (*D–F*), ORF2 protein immunostaining and DAPI counterstaining was performed 6 d post inoculation. The percentage of ORF2 positive cells were quantified based on three independent experiments.

mapping identified that the essential amino acid residues for binding to the cell membrane are located on the surface of the dimeric spike domain.

**HEV-C1$^{VLP}$ Specifically Binds to Liver Tissues as Well as Multiple Regions of Intestine.** HEV is mainly transmitted via the fecal-oral route. The gut epithelium represents the very initial site of virus

**Fig. 4.** Mapping of amino acid residues crucial for the cell-binding of HEV-C1$^{VLP}$. (*A*) Amino acid sequences of HEV-C1 ORF2$^T$. 24 HEV-C1 ORF2$^T$ mutants were created. The amino acid substitutions at the surface of the P2 domain were labeled with red color. (*B*) His-tagged HEV-C1 ORF2$^T$ mutants were expressed and purified. Nondenatured (N) and denatured (D) mutants were analyzed by SDS-PAGE. The images presented are the representative of three independent experiments. (*C*) Structural model of HEV-C1 ORF2$^T$ dimer (*Top* view). The substitutions in the P2 domain essential for VLP formation were shown in cyan. The P2 and truncated P1 domains of the *Right*-side monomer are violet and yellow, whereas the domains on the *Left*-side monomer are light pink and lemon. (*D*) Same as (*B*) for the analysis of nondenatured (N) and denatured (D) mutants. (*E*) The cell-binding of HEV-C1$^{VLP}$ mutants to RH-35 cells was measured by immunofluorescence assay based on three independent experiments. (*F*) The 3D structural model of HEV-C1 ORF2$^T$ dimer (side view). The substitutions in the P2 domain essential for target cell-binding are shown in red.

entry, amplification, and production (29, 30). Notably, HEV-C1$^{VLP}$ efficiently bound to the epithelia of rat duodenum, jejunum, ileum, and colon tissues. This binding could be specifically blocked by anti-HEV-C1$^{VLP}$ sera but not the negative control sera (Fig. 5*A*).

Among the nine mutant VLPs without cell binding affinity, three mutants (M2, M10 and M21) were randomly chosen and subjected to tissue-binding assays. Consistently, these mutants lost binding to rat intestine (Fig. 5*A*). Similar results were observed in rat and liver
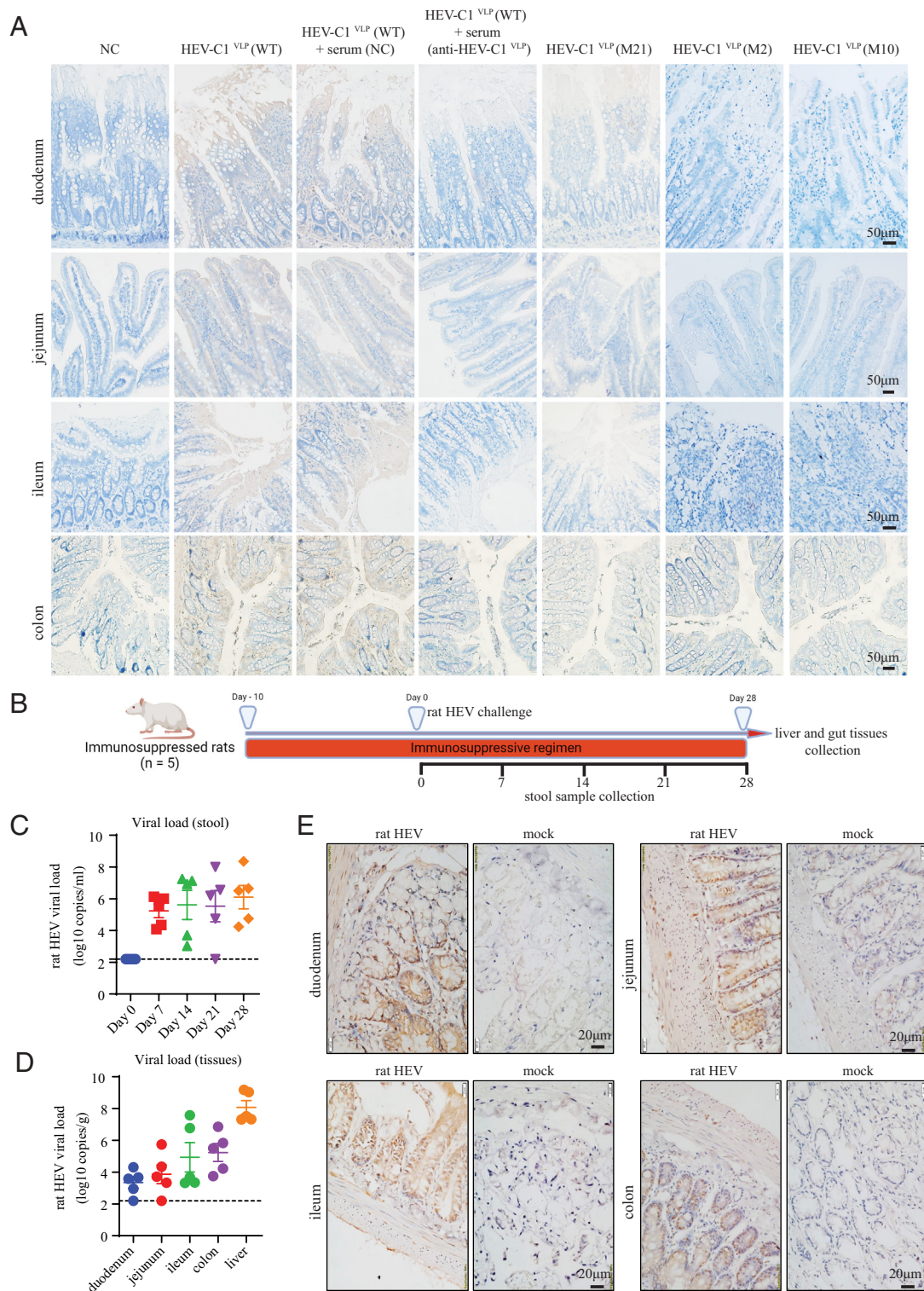
**Fig. 5.** The binding specificity of HEV-C1$^{VLP}$ on live and intestinal tissues. HEV-C1$^{VLP}$ was preincubated with rat NC serum (dilution 1:20) or anti-HEV-C1$^{VLP}$ (dilution 1:20) for 45 min at room temperature. (*A*) rat duodenum, jejunum, ileum, or colon tissue slides were incubated with PBS (NC), HEV-C1$^{VLP}$ (WT), HEV-C1$^{VLP}$ (WT)+ rat NC serum, HEV-C1$^{VLP}$ (WT)+ anti-HEV-C1$^{VLP}$, HEV-C1$^{VLP}$ M21, M2, or M10 overnight at 4 °C. The binding specificity of VLPs was detected by Immunohistochemistry. The images presented are the representative of three independent experiments. (*B*) Scheme of rat infection experiment. Group 1 (n = 5) is given high-dose immunosuppressive drug regimen from −10 d to day 0 and inoculated intravenously with 200ul rat HEV (SRN250811, $10^6$ copies/mL) stool filtrate on day 0, Group 2 (n = 2) rats were administered PBS only on day 0. (*C*) Stool samples were collected on days 0, 7, 14, 21, and 28. The rat HEV viral load were determined by RT-qPCR (n = 5). (*D*) The liver and gut tissues were collected at day 28. Rat HEV viral load was determined by RT-qPCR (n = 5). (*E*) The gut tissues were collected from rat HEV infected rats (n = 5) or mock-infected rats (n = 2) at day 28 and subjected to immunohistochemistry analysis of rat HEV ORF2 protein.

tissue slides (*SI Appendix*, Fig. S16 *A* and *B*), further highlighting the binding specificity of HEV-C1$^{VLP}$ to human target tissue/cells. Two mutants (M23 and M24) that showed intermediate binding on RH-35 cells also possessed moderate binding ability to rat

liver tissue (*SI Appendix*, Fig. S17). More convincingly, the entry of WT HEV-A$^{VLP}$ into HepG2 cells could be efficiently inhibited by anti-HEV-A$^{VLP}$ serum, while its M3 mutant exhibited no entry competence (*SI Appendix*, Fig. S16C). In parallel, the entry of WT

HEV-C1$^{VLP}$ into HepG2 and RH-35 cells was restrained by anti-HEV-C1$^{VLP}$, whereas its M21 mutant possessed no entry potency (*SI Appendix*, Fig. S16 *D and E*). These results highlighted that the surface spike domain of virion capsid dictates the binding and entry of HEV-C1 to its target cells.

In addition, an immunosuppressed rat model was employed to further investigate whether different parts of intestine could support viral replication (Fig. 5*B*) (31). Five rats maintained high HEV-C1 viral loads in stool throughout the experiment with no viral load decline, confirming the establishment of infection in all five rats (Fig. 5*C*). At the end of the experiment, rat livers and different parts of intestine were obtained for viral load testing. Four out of five rats were rat HEV RNA positive in duodenum and jejunum, and all rats were RNA positive in ileum and colon (Fig. 5*D*). More convincingly, immunohistochemical staining showed extensive signals indicative of HEV-C1 antigen expression in the duodenum, jejunum, ileum, colon, and liver of infected rats, whereas no specific staining was observed in mock-infected rats (Fig. 5*E* and *SI Appendix*, Fig. S18). Collectively, these observations imply that rat HEV may initiate infection in multiple regions of the intestine and subsequently cause hepatitis in liver via the gut–liver axis.

**HEV-C1$^{VLP}$ and HEV-A$^{VLP}$ Induce Immune Responses with Partial Bilateral Cross-Reaction.** Although there is the significant zoonotic risk of HEV-C1, the current licensed or experimental HEV vaccines are all based on the recombinant capsid protein derived from a single strain of HEV-A [e.g., the recombinant hepatitis E vaccine Hecolin® is from HEV-1 (28)]. This prompted us to investigate whether a vaccine based on a single HEV-A strain could (partial) cross-inhibit HEV-C1 strains at the cell-binding step. First, we systematically evaluated the antigenic distances of different species by the antigenic cartography. This is a well-established method to inform whether serological cross-inhibition exists among different virus species (32). Herein, VLPs of different species were used to immunize rats and high titers of immune responses were readily detected postimmunization (*SI Appendix*, Fig. S19). This confirmed the good antigenicity of all five VLPs. Next, the interactions between VLPs of HEV A-D and the serially diluted rat sera were measured (*SI Appendix*, Fig. S20). The multidimensional antigenic distances were calculated and projected to the 2D antigenic map (Fig. 6*A*) (33). Interestingly, all VLPs showed an apparent clustering relationship with antigenic distance remotely separated. Exceptionally, the immune response of HEV-A$^{VLP}$ and HEV-C1$^{VLP}$ partially overlaps. This indicates that a partial cross immune relationship exists between these two HEV species.

This observation prompted us to evaluate whether any cross-inhibition exists between HEV-A and HEV-C1. As expected, rat anti-HEV-A$^{VLP}$ sera, but not the negative control sera, efficiently inhibited the binding of HEV-A$^{VLP}$ to HuH7 cell membrane in a dose-dependent manner (Fig. 6 *B* and *C*). Notably, rat anti-HEV-C1$^{VLP}$ sera partially restrained the binding of HEV-A$^{VLP}$ (Fig. 6 *B* and *C*, column 5). Consistently, similar results were observed in HepG2 cells (Fig. 6 *D* and *E*). In addition, anti-HEV-C1$^{VLP}$ sera dose-dependently blocked the binding of HEV-C1$^{VLP}$ to cell membrane (Fig. 6 *F* and *G*). Intriguingly, anti-HEV-A$^{VLP}$ sera also exhibited partial cross-inhibition against the binding of HEV-C1$^{VLP}$ (Fig. 6 *F* and *G*, column 5). However, this inhibition is less efficient compared to its cognate sera, especially when the VLP binding is saturated on the cell membrane (Fig. 6 *H* and *I*). Collectively, we demonstrated that among the different HEV species, HEV-A and HEV-C1 showed cross immune responses and exhibited partial bilateral cross-inhibitory effect at virus binding step.

**HEV-A Patient Sera Cross-React with HEV-C1$^{VLP}$ and Partially Cross-Inhibit HEV-C1$^{VLP}$ Binding.** Sera of acute HEV-A infected (HEV-4) patients were serially diluted and their interaction with VLPs of HEV A-D was measured (*SI Appendix*, Figs. S21 and S22). The multidimensional antigenic distances were calculated and projected to 2D and 3D antigenic maps (*SI Appendix*, Figs. S23 and S24*A*). Consistent with Fig. 6*A*, HEV-A patient sera are distantly separated from the VLPs of HEV-C2, HEV-D, and HEV-B (*SI Appendix*, Fig. S24*A*). In contrast, these sera showed a relatively closer antigenic distance with HEV-C1, albeit with individual variations. According to their positions on the map, human sera were separated into two clusters. One cluster is closer to HEV-C1, while the other is relatively distant.

Next, four sera were randomly selected from each cluster (cluster 1: P1-P4, cluster 2: P5-P8) (*SI Appendix*, Fig. S24*A*). Their inhibitory activity against the binding of both HEV-A$^{VLP}$ and HEV-C1$^{VLP}$ was tested. As expected, seven out of eight HEV-A patient sera, but not the control sera, could dose-dependently inhibit the binding of HEV-A$^{VLP}$ to HepG2 cells, albeit with inter-individual variations (*SI Appendix*, Fig. S24 *B, C, F, and G*). Consistent with Fig. 6 *B–I*, most patient sera partially restrained the binding of HEV-C1$^{VLP}$ (*SI Appendix*, Fig. S24 *D, E, H, and I*), but with some interindividual differences. Collectively, we demonstrated that HEV-A patient sera cross-reacted with HEV-C1$^{VLP}$ and partially cross-inhibited the binding of HEV-C1$^{VLP}$ to its target cells.

**Hecolin® Immunized Human Sera Cross-React with HEV-C1$^{VLP}$ and Partially Cross-Inhibit HEV-C1$^{VLP}$ Binding.** We further investigated whether the licensed human hepatitis E vaccine Hecolin® immunized cohorts could also acquire cross-inhibition against HEV-C1 binding. Hence, sera of 10 individuals who completed Hecolin® immunization were collected. Their interaction with VLPs of HEV A-D species was measured (*SI Appendix*, Fig. S25). The multidimensional antigenic distances were calculated and projected to 2D antigenic maps (*SI Appendix*, Fig. S26*A*). Consistent with Fig. 6*A* and *SI Appendix*, Fig. S24*A*, Hecolin® immunized sera exhibited a closer antigenic distance with HEV-C1, albeit with individual variations (*SI Appendix*, Fig. S26*A*). In line with the efficacy observed in clinic (34), all sera inhibited the cell-binding of HEV-A$^{VLP}$ (*SI Appendix*, Fig. S26 *B, C, F, and G*). Moreover, these sera also partially cross-inhibited the cell-binding of HEV-C1$^{VLP}$. In addition, the inhibitory effect was more pronounced when the concentration of HEV-C1$^{VLP}$ was reduced from 20 to 2.5 μg/mL (*SI Appendix*, Fig. S26 *D, E, H, and I*). These results implied that Hecolin® immunized sera possess partial cross-inhibition against the cell-binding of HEV-C1. Further, the cross-inhibition may become more effective when the amount of HEV-C1 to which a person is exposed is relatively low.

## Discussion

HEV has a plethora of animal reservoirs, and the host range is ever-expanding (35). In fact, HEV is ranked 6th in the risk of animal-to-human spillover among 887 ranked viruses, with its risk potential even proceeding the well-known lethal Marburg virus (ranked 7th) and SARS-CoV (ranked 8th) (36). Classically, human hepatitis E is thought to be exclusively caused by the HEV-A species. However, increasing human cases of HEV-C1 infection have been reported in multiple regions (5–13). The zoonotic potential of these genetically distinct HEV species has raised great public health concerns.
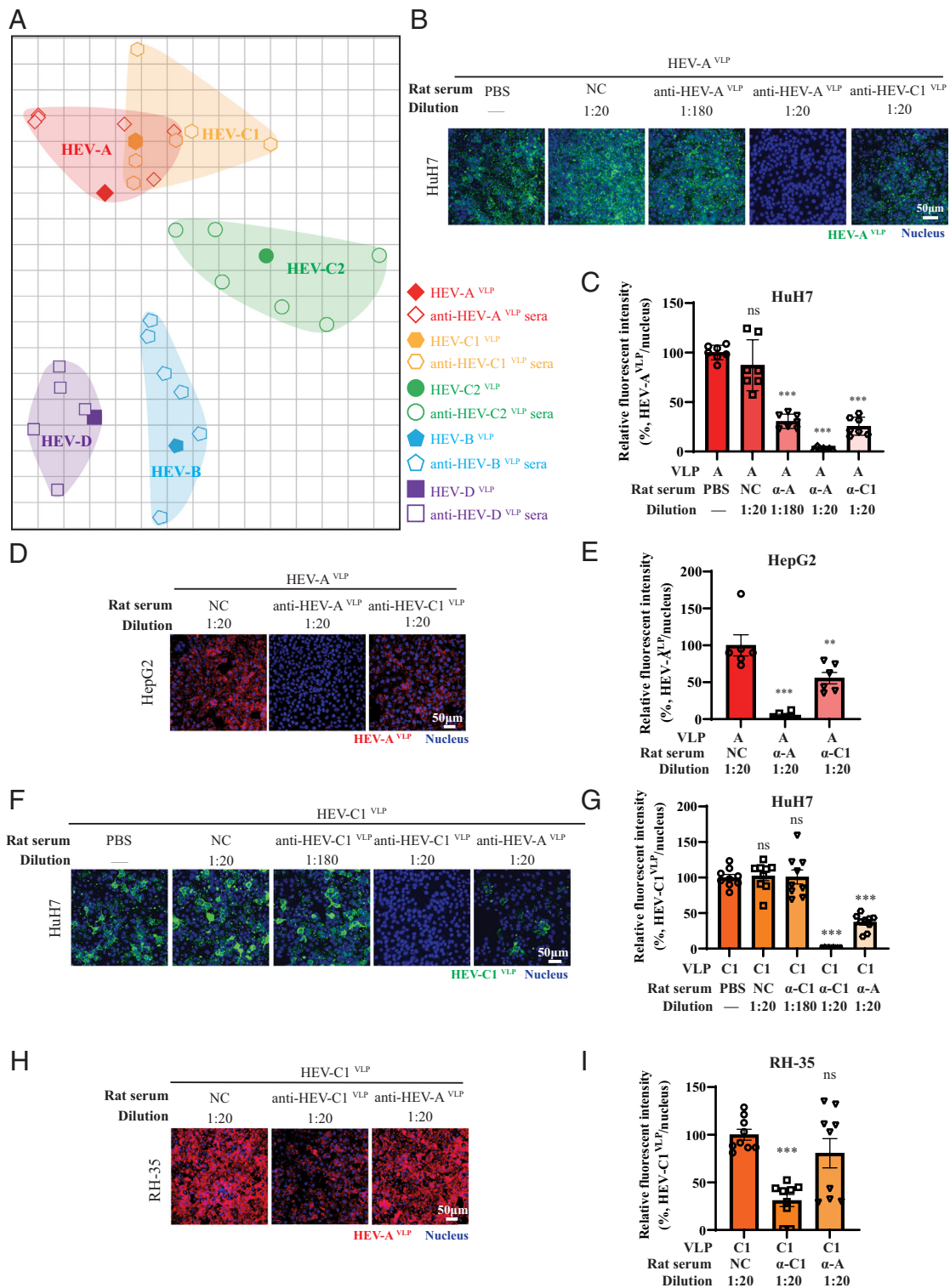
**Fig. 6.** HEV-C1$^{VLP}$ and HEV-A$^{VLP}$ possess closer mutual immune cross-reactivity and partial bilateral cross-protection. (*A*) Two-dimensional antigenic mapping of HEV-A$^{VLP}$, HEV-C1$^{VLP}$, HEV-C2$^{VLP}$, HEV-B$^{VLP}$, and HEV-D$^{VLP}$ with rat sera revealed clustering relationships among different HEV genera. The antigen–antibody cross-reactivity of HEV-A$^{VLP}$ and HEV-C1$^{VLP}$ partially overlaps. The vertical and horizontal axes both represent antigenic distance. One unit of antigenic distance denotes a twofold difference in sera titers. The solid diamond, hexagon, circle, square, and pentagon represent A, C1, C2, B, and D, respectively, whereas the hollow ones correspond to the immunized rat serum of each antigen. (*B* and *C*) HEV-A$^{VLP}$ was preincubated with PBS, rat NC serum (dilution 1:20), rat anti-HEV-A$^{VLP}$ (dilution 1:180 or 1:20), or rat anti-HEV-C1$^{VLP}$ (dilution 1:20). The ability to block the binding of HEV-A$^{VLP}$ to HuH7 cells was detected by immunofluorescence assay. The relative fluorescent intensity was quantified by ImageJ based on three independent experiments. Green, HEV-A $^{VLP}$; blue, nucleus. (*D* and *E*) HEV-A$^{VLP}$ was preincubated with rat NC serum (dilution 1:20), anti-HEV-C1$^{VLP}$ (dilution 1:20), or anti-HEV-A$^{VLP}$ (dilution 1:20). The ability to block the binding of HEV-A$^{VLP}$ to HepG2 cells was measured by immunofluorescence assay. The relative fluorescent intensity was quantified by ImageJ based on three independent experiments. Red, HEV-A $^{VLP}$; blue, nucleus. (*F* and *G*) Same as (*B* and *C*) for testing the ability to block the binding of HEV-C1$^{VLP}$ to HuH7 cells. (*H* and *I*) Same as (*D* and *E*) for testing the ability to block the binding of HEV-C1$^{VLP}$ to RH-35 cells.

****

Viral entry is largely mediated by the specific binding of virions to the bona fide receptor(s) on the cell membrane. It is the first step of virus–host interaction, playing an important role in cell tropism and species specificity (14, 15). It has been well demonstrated that ORF2 (HEV-1 p239, a.a.368 to 606) expressed in *Escherichia coli.* can self-assemble into VLPs, preserving the antigenicity, immunogenicity, virion epitopes and structural features of the outmost moiety of virion (22, 37). This is consistent with the observation that p239 VLP was demonstrated to be an effective prophylactic vaccine Hecolin(®) against HEV-induced hepatitis in large scale clinical trials (28, 34, 38). Thus, the VLPs produced in *E. coli* possess the ability to mimic live viruses in binding host cells. In this study, we found that the corresponding ORF2 (a.a.368 to 606) regions support the assembly of VLPs of all HEV species. More importantly, these VLPs can mimic native HEV particles in cell binding and exhibit specific binding to their cognate liver tissues. Moreover, although the VLPs produced contained a His tag on C terminus, for instance, HEV-A$^{VLP}$, it exhibited similar binding capacity compared with HEV-1$^{VLP}$ (p239 VLP), the main component of human HEV vaccine Hecolin®. The cell binding of both VLPs could be efficiently blocked by anti-HEV-A$^{VLP}$ serum, but not the negative control sera, indicating that His tag exerted no significant effect on cell and antibody binding. Therefore, this complete VLP tool-set enables us to systematically evaluate their cell/tissue binding tropism of different hosts. Strikingly, although significant sequence divergence exists between HEV-A ORF2 and HEV-C1 ORF2, HEV-C1$^{VLP}$ efficiently binds to human-derived liver and intestinal cells/tissues. Moreover, HEV-C1$^{VLP}$ could complete the entry steps and migrate into the human target cells. This observation was further validated by using infectious rat HEV particles. Together with the evidence that human hepatoma cells (e.g., HuH7 and HepG2) support the replication of HEV-C1 (39), our findings elucidated the mechanisms of HEV-C1 zoonosis and explained the infections caused by HEV-C1 in human beings as well as nonhuman primates (5, 6, 12, 40).

In contrast, HEV-B$^{VLP}$ showed no binding and entry capacity, explaining the incompetence of HEV-B to infect nonhuman primates (41). Similarly, HEV-D$^{VLP}$ is also incapable of binding to and entering human cells. This implies that the zoonotic potential of HEV-D is low at present. Nevertheless, bats 1) are the second-largest order of mammals after rodents, widely inhabiting all continents except Antarctica, 2) possess extraordinary immune tolerance to support host–virus coexistence in an equilibrium pattern, and 3) have a large and closely aggregated population with extreme roosting closeness and sustained flight capability (42). Thus, bats can sustain virus infection and transmission, endow virus with high probability to accumulate mutations, produce variants acquired adaptation to other hosts, and cause spillover infection in humans (43). Consequently, the potential of interspecies transmission of HEV-D merits continued surveillance and investigation. Interestingly, HEV-C2$^{VLP}$ showed residual binding and entry toward human as well as rat cell lines, albeit its relatively closer relationship with HEV-C1. This explained the incapability of HEV-C2 to infect nonhuman primates as well as rats (at least at the cell entry steps) (44), implying that HEV-C2 possesses limited (if exists) zoonotic risk at present.

Point mutations of VLPs based on the crystal structure analysis represents a valuable method to identify the specific molecular determinants on virion that mediate VLP formation and binding to cell membrane (21, 45). By constructing a series of HEV-C1 VLP mutants, we identified that multiple residues of the spike domain are crucial for VLP formation or binding to the target cell membrane. Interestingly, those residues essential for cell binding are dispersed on the apical surface as well as the horizontal region of the spike domain. The residues located on the apical surface may directly bind to the cell membrane, while those on the horizontal region may have an allosteric effect, inducing conformational changes of the spike domain to indirectly mediate the binding process. In short, the spike domains interact directly with the cellular receptor(s) of HEV-C1. Similarly, the spike domain of HEV-A was reported to be essential for cell binding affinity (21). Nevertheless, due to the sequence divergence between these two species, we postulate that HEV-A and HEV-C1 may employ different cellular receptor(s) to mediate their entry. However, the bona fide receptor(s) of both HEV species remain unknown. The identification of their receptors would be essential to further elucidate the detailed process of virus entry, as well as the coevolution and coadaption landscapes between different HEV species and their hosts.

Although HEV is a hepatotropic virus, it is mainly transmitted via the fecal-oral route. The gut epithelium represents the very initial site of virus entry, amplification, and production (29, 30). In this study, we observed the specific binding of HEV-C1$^{VLP}$ to different parts of rat intestine. More convincingly, HEV-C1 positive cells were readily detected in duodenum, jejunum, ileum, and colon tissues of rat HEV infection animal model. Notably, HEV-A antigen has been detected in multiple regions of the intestine in infected patients (30). Similarly, the replicative viral RNA of HEV-B was detected in avian gastrointestinal tissues, including the colorectal, cecal, jejunal, ileal, duodenal, and cecal tonsil tissues. All these observations suggest that HEV species may penetrate the gut from multiple parts of the intestine, but not a specific intestinal region, to initiate its infection. Subsequently, HEV may take advantage of the gut–liver axis to infect hepatocytes through portal circulation (46). The lipid-coated virions are delipidated into nHEV in the intestine and the biliary tract. These highly infectious and stable virions render the outstanding transmission capacity of HEV enterically, causing hepatitis E outbreaks periodically around the world (1). Currently, the transmission source of HEV-C1 from rats to humans is still unknown. Importantly, we found that HEV-C1$^{VLP}$ bound efficiently to human intestinal and liver tissues. This indicates that the cross-species transmission of HEV-C1 from rat to human may also be achieved via the fecal-oral route. Therefore, the contamination of food products may be a possibility of transmission source.

This study comparatively mapped the antigenic cartography of different HEV species. All species exhibited a clustering relationship with antigenicity distantly separated. Exceptionally, a closer bilateral cross-reactive relationship was observed between HEV-A and HEV-C1. This echoes the fact that the commercial HEV-A serological detection kits are positive for a portion of HEV-C1 sera, but with less sensitivity (47). Therefore, species-specific diagnostic methods are needed for the detection of HEV-C1 infections (48, 49). Importantly, a partial bilateral cross-protective relationship was observed between HEV-A and HEV-C1. This explains why prior vaccination with HEV-A antigen can provide partial protection against HEV-C1 infection in rats (47). In addition, both HEV-A patient sera and HEV vaccine Hecolin® immunized human sera showed partial cross-inhibition against HEV-C1 at the virus binding step. Notably, the estimated anti-HEV-A IgG seroprevalence is about 12.47% among the general population (50). Whether (or to what extent) the partial cross-protection of HEV-A antibodies would affect the prevalence of HEV-C1 in human populations merits further investigation. Currently, the exact data on the global burden of zoonotic HEV-C1 infection remains largely elusive, although several large-scale screenings have been done (51–53). In Europe and Asia, HEV-C1 RNA was

frequently detected in rats with a prevalence up to 27.2% (53). Therefore, the zoonotic risk of HEV-C1 to human populations should never be ignored.

Our study has several limitations. The robust cell culture systems have been established only for certain HEV strains (e.g., HEV-3 and HEV-4) (20, 54), not for all HEV A-D species. Therefore, we generated VLPs of HEV A-D species and comparatively assessed their binding host tropism. VLPs are believed to be a good model to mimic live viruses in binding and penetrating host cells (23, 24), however the possible differences [e.g., particle size and glycosylation modification (55)] in comparison to authentic viruses should be noted. The binding specificity of HEV-C1 VLPs was validated with infectious rat HEV in our study. Second, most of the HEV-related reverse genetics systems (RGSs) developed so far are limited because of slowly replicating viruses and low virus recovery rates (56). RGSs producing high virus titers are almost restricted to HEV-3 so far. To further validate the key residues on HEV-C1$^{VLP}$ that are essential for cell binding, we tried to use the site-directed mutagenesis approach based on a full-length rat HEV (strain LCK-3110) RGS to harvest mutant rat HEV virions. However, we could not obtain enough mutant rat HEV to perform the virus binding assays probably due to the relatively lower viral replication efficiency and the high sensitivity of HEV genomes to nucleotide mismatches (56–60).

In summary, the direct interactions between the viral capsid and cellular receptor(s) regulate the distinct zoonotic potentials of different HEV species (*SI Appendix*, Fig. S27). The systematic characterization of antigenic cartography and serological cross-reactivity of different HEV species provide valuable insights for the development of species-specific diagnosis and protective vaccines against zoonotic HEV infection.

## Materials and Methods

The usage of human serum and tissues samples for research was approved by the Scientific and Ethics Committee of the Affiliated Hospital of Xuzhou Medical University (reference number XYFY2022-KL113-02 and XYFY2023-KL353-01), with the informed consent waived by the committee due to the reuse of specimens obtained from previous clinical diagnosis or treatment (with the personal information or identity removed). The utilization of HEV vaccine

Hecolin® immunized human sera was in accordance with ethics approval (No. SPHIRB-201903) (34), with informed consent from donors. Sera were tested IgG or IgM positive with the Wantai HEV kit and our in-house HEV-A ORF2$^{VLP}$ ELISA kit. The ORF2 proteins were expressed in *E. coli* strain BL21 and purified by Ni-NTA affinity chromatography column (Solarbio). Cells were maintained in Dulbecco's modified Eagle's MEM (Biochannel, Sbjbio) supplemented with 10% FBS (Biochannel, Sbjbio). The detailed materials and methods are provided in *SI Appendix*.

**Data, Materials, and Software Availability.** All study data are included in the article and/or supporting information.

Author affiliations: ªDepartment of Pathogen Biology and Immunology, Jiangsu Key Laboratory of Immunity and Metabolism, Jiangsu International Laboratory of Immunity and Metabolism, Xuzhou Medical University, Xuzhou 221004, China; ᵇDepartment of Microbiology, School of Clinical Medicine, Li Ka Shing Faculty of Medicine, The University of Hong Kong, Pokfulam, Hong Kong, China; ᶜDepartment of Infectious Diseases, The Affiliated Hospital of Xuzhou Medical University, Xuzhou 221002, China; ᵈState Key Laboratory of Molecular Vaccinology and Molecular Diagnostics, National Institute of Diagnostics and Vaccine Development in Infectious Diseases, School of Public Health, School of Life Sciences, Xiamen University, Xiamen 361102, China; ᵉChinese Academy of Sciences Key Laboratory of Special Pathogens and Biosafety, Wuhan Institute of Virology, Chinese Academy of Sciences, Wuhan 430207, China; ᶠGuangzhou Laboratory, Guangzhou International Bio Island, Guangzhou 510320, China; ᵍDepartment of Epidemiology, Ministry of Education Key Laboratory of Public Health Safety, School of Public Health, Fudan University, Shanghai 200032, China; and ʰState Key Laboratory of Veterinary Biotechnology, Harbin Veterinary Research Institute, the Chinese Academy of Agricultural Sciences, Harbin 150069, China

Author contributions: H.G., K.Z., X.P., S.S., and W.W. designed research; H.G., J.X., J.S., C.L., X.W., Y.H., G.Y., L.W., D.Y., Z.L., Z.W., J.S., D.Z., J.Z., X.D., S.W., W.M., and S.S. performed research; X.W., G.Y., D.Y., J.S., Y.D., R.T., Y.L., H.K., P.Z., Z.Z., and X.P. contributed new reagents/analytic tools; H.G., J.X., J.S., C.L., Y.H., L.W., Z.L., Z.W., Y.D., D.Z., J.Z., X.D., R.T., K.Z., S.S., and W.W. analyzed data; and H.G. and W.W. wrote the paper.

1. A. N. Desai et al., Viral hepatitis E outbreaks in refugees and internally displaced populations, sub-Saharan Africa, 2010–2020. *Emerg. Infect. Dis.* **28**, 1074–1076 (2022).
2. B. Wang, X. J. Meng, Hepatitis E virus: Host tropism and zoonotic infection. *Curr. Opin. Microbiol.* **59**, 8–15 (2021).
3. M. A. Purdy et al., ICTV virus taxonomy profile: Hepeviridae 2022. *J. Gen. Virol.* **103**, 001778 (2022).
4. D. B. Smith et al., Consensus proposals for classification of the family Hepeviridae. *J. Gen. Virol.* **95**, 2223–2232 (2014).
5. A. Andonov et al., Rat hepatitis E virus linked to severe acute hepatitis in an immunocompetent patient. *J. Infect. Dis.* **220**, 951–955 (2019).
6. S. Sridhar et al., Transmission of rat hepatitis E virus infection to humans in Hong Kong: A clinical and epidemiological analysis. *Hepatology* **73**, 10–22 (2021).
7. A. Rivero-Juarez et al., Orthohepevirus C infection as an emerging cause of acute hepatitis in Spain: First report in Europe. *J. Hepatol.* **77**, 326–331 (2022).
8. S. Sridhar et al., Hepatitis E virus species C infection in humans, Hong Kong. *Clin. Infect. Dis.* **75**, 288–296 (2022).
9. C. Rodriguez, S. Marchand, A. Sessa, P. Cappy, J. M. Pawlotsky, Orthohepevirus C hepatitis, an underdiagnosed disease? *J. Hepatol.* **79**, e39–e41 (2023).
10. M. Casares-Jimenez et al., Correlation of hepatitis E and rat hepatitis E viruses urban wastewater monitoring and clinical cases. *Sci. Total Environ.* **908**, 168203 (2024).
11. M. Casares-Jimenez et al., Rat hepatitis E virus (Rocahepevirus ratti) in people living with HIV. *Emerg. Microbes Infect.* **13**, 2295389 (2024).
12. S. Sridhar et al., Rat hepatitis E virus as cause of persistent hepatitis after liver transplant. *Emerg. Infect. Dis.* **24**, 2241–2250 (2018).
13. J. Caballero-Gomez et al., Acute hepatitis in children due to rat hepatitis E virus. *J. Pediatr.* **273**, 114125 (2024).
14. L. W. Meredith, G. K. Wilson, N. F. Fletcher, J. A. McKeating, Hepatitis C virus entry: Beyond receptors. *Rev. Med. Virol.* **22**, 182–193 (2012).
15. T. F. Baumert et al., Entry of hepatitis B and C viruses–Recent progress and future impact. *Curr. Opin. Virol.* **4**, 58–65 (2014).
16. X. Yin, Z. Feng, Hepatitis E virus entry. *Viruses* **11**, 883 (2019).
17. X. Yin, C. Ambardekar, Y. Lu, Z. Feng, Distinct entry mechanisms for nonenveloped and quasi-enveloped hepatitis E viruses. *J. Virol.* **90**, 4232–4242 (2016).
18. M. I. Costafreda, S. Sauleda, A. Rico, M. Piron, M. Bes, Detection of nonenveloped hepatitis E virus in plasma of infected blood donors. *J. Infect. Dis.* **226**, 1753–1760 (2022).
19. T. L. Meister, J. Bruening, D. Todt, E. Steinmann, Cell culture systems for the study of hepatitis E virus. *Antiviral. Res.* **163**, 34–49 (2019).
20. N. Chew, J. Situ, S. Wu, W. Yao, S. Sridhar, Independent evaluation of cell culture systems for hepatitis E virus. *Viruses* **14**, 1254 (2022).
21. T. Yamashita et al., Biological and immunological characteristics of hepatitis E virus-like particles based on the crystal structure. *Proc. Natl. Acad. Sci. U.S.A.* **106**, 12986–12991 (2009).
22. S. W. Li et al., The development of a recombinant hepatitis E vaccine HEV 239. *Hum. Vaccin. Immunother.* **11**, 908–914 (2015).
23. T. S. Guu et al., Structure of the hepatitis E virus-like particle suggests mechanisms for virus assembly and receptor binding. *Proc. Natl. Acad. Sci. U.S.A.* **106**, 12992–12997 (2009).
24. S. Li et al., Dimerization of hepatitis E virus capsid protein E2s domain is essential for virus-host interaction. *PLoS Pathog.* **5**, e1000537 (2009).
25. S. He et al., Putative receptor-binding sites of hepatitis E virus. *J. Gen. Virol.* **89**, 245–249 (2008).
26. D. B. Smith et al., Update: Proposed reference sequences for subtypes of hepatitis E virus (species Orthohepevirus A). *J. Gen. Virol.* **101**, 692–698 (2020).
27. D. B. Smith et al., Proposed reference sequences for hepatitis E virus subtypes. *J. Gen. Virol.* **97**, 537–542 (2016).
28. F. C. Zhu et al., Efficacy and safety of a recombinant hepatitis E vaccine in healthy adults: A large-scale, randomised, double-blind placebo-controlled, phase 3 trial. *Lancet* **376**, 895–902 (2010).
29. T. P. Williams et al., Evidence of extrahepatic sites of replication of the hepatitis E virus in a swine model. *J. Clin. Microbiol.* **39**, 3040–3046 (2001).
30. O. Marion et al., Hepatitis E virus replication in human intestinal cells. *Gut* **69**, 901–910 (2020).
31. S. Sridhar et al., A small animal model of chronic hepatitis E infection using immunocompromised rats. *JHEP Rep.* **4**, 100546 (2022).

32. I. Sitaras, Antigenic cartography: Overview and current developments. *Methods Mol. Biol.* **2123**, 61–68 (2020).
33. D. J. Smith *et al.*, Mapping the antigenic and genetic evolution of influenza virus. *Science* **305**, 371–376 (2004).
34. J. Zhang *et al.*, Long-term efficacy of a hepatitis E vaccine. *N. Engl. J. Med.* **372**, 914–922 (2015).
35. X. J. Meng, Expanding host range and cross-species infection of hepatitis E virus. *PLoS Pathog.* **12**, e1005695 (2016).
36. Z. L. Grange *et al.*, Ranking the risk of animal-to-human spillover for newly discovered viruses. *Proc. Natl. Acad. Sci. U.S.A.* **118**, e2002324118 (2021).
37. M. Wei *et al.*, Bacteria expressed hepatitis E virus capsid proteins maintain virion-like epitopes. *Vaccine* **32**, 2859–2865 (2014).
38. G. Zhong *et al.*, Safety of hepatitis E vaccination for pregnancy: A post-hoc analysis of a randomized, double-blind, controlled phase 3 clinical trial. *Emerg. Microbes Infect.* **12**, 2185456 (2023).
39. Y. Debing *et al.*, A rat model for hepatitis E virus. *Dis. Model Mech.* **9**, 1203–1210 (2016).
40. F. Yang *et al.*, Experimental cross-species transmission of rat hepatitis E virus to rhesus and cynomolgus monkeys. *Viruses* **14**, 293 (2022).
41. F. F. Huang *et al.*, Determination and analysis of the complete genomic sequence of avian hepatitis E virus (avian HEV) and attempts to infect rhesus monkeys with avian HEV. *J. Gen. Virol.* **85**, 1609–1618 (2004).
42. D. Jebb *et al.*, Six reference-quality genomes reveal evolution of bat adaptations. *Nature* **583**, 578–584 (2020).
43. F. L. Roes, On the evolution of virulent zoonotic viruses in bats. *Biol. Theory* **15**, 223–225 (2020).
44. T. C. Li *et al.*, Monkeys and rats are not susceptible to ferret hepatitis E virus infection. *Intervirology* **58**, 139–142 (2015).
45. J. D. Fiedler *et al.*, Engineered mutations change the structure and stability of a virus-like particle. *Biomacromolecules* **13**, 2339–2348 (2012).
46. N. Oechslin, D. Moradpour, J. Gouttenoire, Hepatitis E virus finds its path through the gut. *Gut* **69**, 796–798 (2020).
47. S. Sridhar *et al.*, Multimodal investigation of rat hepatitis E virus antigenicity: Implications for infection, diagnostics, and vaccine efficacy. *J. Hepatol.* **74**, 1315–1324 (2021).
48. Z. Chen *et al.*, Redeveloping antigen detection kits for the diagnosis of rat hepatitis E virus. *J. Clin. Microbiol.* **61**, e0071023 (2023).
49. J. Situ *et al.*, An immunoassay system to investigate epidemiology of Rocahepevirus ratti (rat hepatitis E virus) infection in humans. *JHEP Rep.* **5**, 100793 (2023).
50. P. Li *et al.*, The global epidemiology of hepatitis E virus infection: A systematic review and meta-analysis. *Liver Int.* **40**, 1516–1528 (2020).
51. M. Faber, J. J. Wenzel, M. Erl, K. Stark, M. Schemmerer, No evidence for orthohepevirus C in archived human samples in Germany, 2000–2020. *Viruses* **14**, 742 (2022).
52. P. Pankovics *et al.*, Four-year long (2014–2017) clinical and laboratory surveillance of hepatitis E virus infections using combined antibody, molecular, antigen and avidity detection methods: Increasing incidence and chronic HEV case in Hungary. *J. Clin. Virol.* **124**, 104284 (2020).
53. D. Parraud *et al.*, Rat hepatitis E virus: Presence in humans in South-Western France? *Front. Med. (Lausanne)* **8**, 726363 (2021).
54. D. Todt *et al.*, Robust hepatitis E virus infection and transcriptional response in human hepatocytes. *Proc. Natl. Acad. Sci. U.S.A.* **117**, 1731–1741 (2020).
55. M. Ankavay *et al.*, New insights into the ORF2 capsid protein, a key player of the hepatitis E virus lifecycle. *Sci. Rep.* **9**, 6243 (2019).
56. J. Scholz, A. Falkenhagen, C. T. Bock, R. Johne, Reverse genetics approaches for hepatitis E virus and related viruses. *Curr. Opin. Virol.* **44**, 121–128 (2020).
57. J. Scholz *et al.*, Establishment of a plasmid-based reverse genetics system for the cell culture-adapted hepatitis E virus genotype 3c strain 47832c. *Pathogens* **9**, 157 (2020).
58. Y. W. Huang *et al.*, Capped RNA transcripts of full-length cDNA clones of swine hepatitis E virus are replication competent when transfected into Huh7 cells and infectious when intrahepatically inoculated into pigs. *J. Virol.* **79**, 1552–1558 (2005).
59. P. Shukla *et al.*, Adaptation of a genotype 3 hepatitis E virus to efficient growth in cell culture depends on an inserted human gene segment acquired by recombination. *J. Virol.* **86**, 5697–5707 (2012).
60. X. Ju *et al.*, Identification of functional cis-acting RNA elements in the hepatitis E virus genome required for viral replication. *PLoS Pathog.* **16**, e1008488 (2020).

1 **Supplementary documents**

2 **Cell binding tropism of rat hepatitis E virus is a pivotal**

3 **determinant of its zoonotic transmission to humans**

4 **Table of contents**

9

10

11

**Supplementary materials and methods**

**Plasmids**

The nucleotide sequences encoding the five truncated ORF2 proteins (HEV-A ORF2$^T$ to HEV-D ORF2$^T$) were synthesized by GENEWIZ and inserted into pET-21a (+) empty vector with his tag located at C terminus. The five plasmids were named pET-21a (+) – HEV-A ORF2$^T$, pET-21a (+) – HEV-C1 ORF2$^T$, pET-21a (+) – HEV-C2 ORF2$^T$, pET-21a (+) – HEV-B ORF2$^T$ and pET-21a (+) – HEV-D ORF2$^T$. Based on pET-21a (+) – HEV-A ORF2$^T$ plasmid, three HEV-A ORF2$^T$ mutant plasmids (M1, M2 and M3) were generated by PCR based site-directed mutagenesis. In parallel, 24 HEV-C1 ORF2$^T$ mutant plasmids (M1-M24) were generated based on pET-21a (+) – HEV-C1 ORF2$^T$.

**Production of his-tagged truncated ORF2 proteins and assembly of virus-like particles (VLPs)**

The proteins were expressed with C-terminally 6×his tag in E. coli strain BL21 (DE3) and were purified by Ni-NTA affinity chromatography column (Solarbio, Beijing, China). The purified proteins were further dialyzed at 4℃ overnight and checked by SDS-PAGE. Assembled proteins were stained with 1.5% Uranium acetate solution (pH 7.0) over carbon-coated copper grids and photographed using a Tecnai G2 Spirit Twin transmission electron microscope (FEI, Hillsboro, OR, USA).

**3D structural model**

The crystal structure of Hepatitis E virus genotype 1 isolate Human/Burma (Protein Data Bank accession no. 2ZZQ) was used as a template for modeling the structures of HEV-A ORF2 and HEV-C1 ORF2 proteins with SWISS-MODEL (https://swissmodel.expasy.org). The structures of wild-type and mutant ORF2 proteins were visualized and analyzed by PyMOL (version 2.5.4).

**Sample preparation**

41     SD rats (Rattus norvegicus, SPF level, average weight: 170~190 g) were injected

42     subcutaneously with 200 μg of HEV-A ORF2$^T$, HEV-C1 ORF2$^T$, HEV-C2 ORF2$^T$, HEV-B

43     ORF2$^T$, HEV-D ORF2$^T$ or PBS (mixed with adjuvant aluminum hydroxide) with 2 weeks

44     intervals. Serum samples were collected pre- and post-immunization. Ethics approval for these

45     animal-related experiments was obtained from the Institutional Animal Care and Use

46     Committee of Xuzhou Medical University (Approval No. 202111A115). The usage of chicken

47     and ferret liver samples was approved by the Committee on the Ethics of Animal Experiments

48     of the HVRI of CAAS (Approval number 2020-01-01JiPi, 220518-02-GR). Bat liver tissue

49     samples collected from horseshoe bat (*Rhinolophus*)(1) was used in accordance with ethics

50     approval of animal welfare committee of WIV (WIVA05202204).

51

52     **Cell binding assay**

53     HuH7, HepG2, Caco2 and RH-35 cells were maintained in Dulbecco's modified Eagle's MEM

54     (Biochannel, Sbjbio) supplemented with 10% FBS (Biochannel, Sbjbio). When confluency

55     reached 80%, cells were washed with pre-chilled 1×PBS. Next, cells were incubated with wild-

56     type or mutant VLPs (20 μg/ml, if not specified) or 1×PBS (negative control) for 1h at 4°C with

57     slow shaking on a rotator. After removing the supernatant, cells were extensively washed with

58     ice-cold 1×PBS for 3-4 times to remove unbound VLPs. For IF staining, cells were fixed with

59     4% PFA, and then incubated with antibodies diluted in 2% BSA. The primary antibodies used

60     are described below. Rabbit anti-HEV-A$^{VLP}$ polyclonal antibodies, anti-HEV-B$^{VLP}$ polyclonal

61     antibodies, anti-HEV-C1$^{VLP}$ polyclonal antibodies, anti-HEV-C2$^{VLP}$ polyclonal antibodies and

62     anti-HEV-D$^{VLP}$ polyclonal antibodies were developed in our lab. His-tag mouse monoclonal

63     antibody was purchased from Proteintech (66005-1-Ig). CoraLite594-conjugated Goat Anti-

64     Rabbit IgG(H+L) (Proteintech, SA00013-4) or CoraLite488-conjugated Goat Anti-Rabbit

65     IgG(H+L) (Proteintech, SA00013-2) were used as secondary antibody. Nuclei were stained

66     with Hoechst Stains (Invitrogen, USA). Fluorescent images were captured by Olympus

67     fluorescent microscope (model U-LH100HGAPO). For each independent experiment, the

68     fluorescent images were taken from random areas with the same parameters set on the

69     microscopy (e.g., image resolution, imaging speed and acquisition time). For each image, the

3

70  fluorescence intensity of two independent channels (one for the nucleus, the other for the

71  detected protein) were quantified separately by ImageJ software. The fluorescent intensity of

72  the detected protein was further normalized by its nucleus fluorescent intensity to exclude the

73  possible interference of varied cell numbers captured in the images.

74

75  **Antigenic cartography**

76  The antigen-antibody reactivity between VLPs of HEV genera and rat/human sera was

77  measured by ELISA. HEV-A$^{VLP}$, HEV-C1$^{VLP}$, HEV-C2$^{VLP}$, HEV-D$^{VLP}$ and HEV-B$^{VLP}$ were used

78  as the foundation of the antigenic cartography. The dilution factors of sera which reach 50% of

79  maximum antigen-sera interaction were used to calculate the antigenic distance. The dilution

80  factors were converted into a Log scale. The highest value of five antigens against one serum

81  was defined as column base, and the antigenic distance equals to the subtraction of column

82  bases and log dilution factors, as higher values indicate more dissimilarity on the

83  multidimensional scaling map. The 2D antigenic map projection was described by Smith et

84  al.,(2) and generated via the ACMACS antigenic cartography algorithm (https://acmacs-

85  web.antigenic-cartography.org). Each unit of antigenic distance (grid lines) denotes a twofold

86  difference in serum titers. The 3D cartographic projections were generated using Racmacs

87  1.1.35. Antigenic distance and coordinates data were separately downloaded from Racmacs.

88  3D coordinates data of HEV-B$^{VLP}$ was converted into $[x, y, z] = [0, 0, 0]$, and other 3D

89  coordinates data sets of antigens and sera were transformed correspondingly using 3D rotation

90  conversion formula. The 3D antigenic maps were drawn by 3D plot function of OriginPro 2021

91  software (9.8.0.200).

92

93  **VLPs entry assay**

94  HepG2 and RH35 cells ($4 \times 10^4$) were seeded on slides in 48-well plates one day before. VLPs

95  (60 µg/million cells) were added to chilled cells on ice for 1 h, then washed four times with ice-

96  cold PBS and shifted to 37°C prewarmed complete medium for 1h. After internalization, cells

97  were fixed and incubated with antibodies diluted in 2% BSA. His-tag mouse monoclonal

98  antibody was used as the primary antibody (Proteintech, 66005-1-Ig). Alexa Fluor® 594

4

99　　AffiniPure Goat Anti-Mouse IgG (H+L) (Jackson, 115-585-003) was used as the secondary

100　　antibody. Hoechst was used to stain the nucleus. Fluorescent images were captured using a laser

101　　scanning confocal microscope (Leica STELLARIS 5, Germany). Additionally, bright field

102　　microscopy channel was used to determine outlines of adherent cells. Cell boundary was

103　　illustrated with white dash lines. The red dots within the cell boundary were counted and

104　　quantified to determine the VLP entry efficiency.

105

106　　**Virus entry assay**

107　　rat HEV (SRN250811) and human HEV-3 (Kernow-C1/p6) infectious viruses were prepared as

108　　previously described (3) (4). HepG2 and RH35 cells ($4 \times 10^4$ cells/well) were seeded onto 8

109　　mm slides (Xinyou, 050810) in 48-well plates one day before infection. If not specified, cells

110　　were inoculated with rat HEV ($1 \times 10^4$ copy numbers/cell) or human HEV ($1 \times 10^4$ copy

111　　numbers/cell) for 1 h at 37°C, washed extensively with PBS 3-4 times, and fixed for

112　　visualization by confocal microscopy (Leica STELLARIS 5, Germany). Rabbit anti-HEV-A$^{VLP}$

113　　polyclonal antibodies and anti-HEV-C1$^{VLP}$ polyclonal antibodies were used as primary

114　　antibodies, respectively. Alexa Fluor® 594 AffiniPure Goat Anti-Rabbit IgG (H+L) (Jackson,

115　　111-585-003) was used as the secondary antibody. Hoechst was used to stain the nucleus.

116　　Fluorescent images were captured using a laser scanning confocal microscope (Leica

117　　STELLARIS 5, Germany). In addition, bright field microscopy channel was used to determine

118　　outlines of adherent cells. Cell boundary was illustrated with white dash lines. The red dots

119　　within the cell boundary were counted and quantified to determine the virus entry efficiency.

120

121　　**Rat infection experiment**

122　　Female, 6–8 weeks old, specific-pathogen-free Sprague–Dawley rats (*Rattus norvegicus*) were

123　　obtained from the Center for Comparative Medical Research of The University of Hong Kong.

124　　Ethics approval for the study was obtained from the Committee on the Use of Live Animals in

125　　Teaching and Research of The University of Hong Kong (protocol: 4817-18). Rats were housed

126　　in a biosafety level 2 animal facility and had access to standard pellet feed and water *ad libitum*.

127　　Rats were divided into two groups: Group 1 (n = 5) was given high-dose immunosuppressive

drug regimen as described previously (3) from -10 day post inoculation to end of experiment

and inoculated intravenously with 200ul rat HEV (SRN250811, $10^6$ copies/mL) stool filtrate on

the day of infection (day 0), Group 2 (n = 2) rats were administered PBS only on the day of

infection (day 0). Stool samples were collected on designated days (day 0, 7, 14, 21 and 28)

and tested by RT-qPCR (HEV-C1). The liver and gut tissues (duodenum, jejunum, ileum and

colon) were collected at day 28 for RT-qPCR (HEV-C1) and immunohistochemistry assays as

described previously (3).


**RT-qPCR**

HepG2 and RH-35 cells ($3\times10^4$ cells/well) were seeded onto 48 well plates one day before

infection. Cells were inoculated with rat HEV ($4\times10^7$ copy numbers/well) or human HEV-3 (1

$\times10^8$ copy numbers/well) overnight at 37°C, washed extensively with PBS for 4 times and refed

with DMEM supplemented with 10% FBS. Total RNA was isolated from cell lysates 6 days

post infection. Real-time qRT-PCR was performed to quantify the HEV RNA using ABScript

III One Step RT-qPCR Probe Kit with UDG V5 (Abclonal, RK20412). The primers for human

HEV RNA were 5'-AATAAATCATAAGTGGTTTCTGGGGTGAC-3' (forward primer), 5'-

AATAAATCATAA GGRTTGGTTGGRTGAA-3' (reverse primer), and 5'-FAM-G*

TGATTCTCAGCCCTTCG-MGB-NFQ-3' (probe) (5). The primers for rat HEV RNA were 5'-

CTTGTTGAGCTYTTYTCCCCT-3' (forward primer), 5'-CTGTAYCGGATGCGACCAA-3'

(reverse primer), and 5'-FAM-TGCAGCTTGTCTTTGARCC-MGB-NFQ-3' (probe) (6).

(R=A or G; Y=C or T)


**Immunohistochemistry**

Formalin-fixed, paraffin-embedded tissues were sectioned at a thickness of 3 μm. Tissue

sections were deparaffinized and rehydrated, and antigens were retrieved by boiling in 10 mM

sodium citrate (pH 6.0) for 8-10 min. Endogenous peroxidase was inactivated by 3% hydrogen

peroxide for 30 min at room temperature (RT), and after washing with phosphate-buffered

saline (PBS)–0.1% Tween (PBST), the slides were blocked with 10% normal goat serum for 30

min at RT. To detect the binding of VLPs to tissues, VLPs (20 μg/mL) or 1×PBS (negative

control) were incubated overnight at 4°C. The slides were rinsed three times in PBS, then incubated with peroxidase-conjugated affinipure rabbit anti-his tag antibody (Jackson, 300-035-240). The binding was visualized by the DAB kit (ZSGB-BIO, ZLI-9019). After counterstaining with hematoxylin, images were taken with an Olympus IX51 inverted microscope.

**Western blot**

Non-denatured samples were prepared with non-denatured gel sample loading buffer (unboiled). Denatured samples were prepared with normal sample loading buffer (boiled). Cell lysates were applied to SDS-PAGE gels. Proteins were transferred onto nitrocellulose membranes by semidry transfer and incubated with primary antibodies as indicated below. Rabbit anti-HEV-A$^{VLP}$ polyclonal antibodies, anti-HEV-C1$^{VLP}$ polyclonal antibodies, anti-HEV-C2$^{VLP}$ polyclonal antibodies, anti-HEV-D$^{VLP}$ polyclonal antibodies and anti-HEV-B$^{VLP}$ polyclonal antibodies were developed in our lab. His-tag mouse monoclonal antibody was purchased from Proteintech (66005-1-Ig). IRDye 800CW Goat anti-Rabbit IgG (H+L) (Licor, 926-32211), IRDye 680RD Goat anti-Mouse IgG (H+L) (Licor, 926-68070) or HRP-conjugated Affinipure Goat Anti-Rat IgG(H+L) (Proteintech, SA00001-15) were used as secondary antibody.

**Statistical analysis**

Graphs were generated using GraphPad Prism 9 (GraphPad software Inc). All error bars throughout the study represent the standard deviation (SD). Comparison between two groups was determined using unpaired two-tailed Student's t-test, comparison between multiple groups was performed with a One-Way ANOVA with Post Hoc Tests (*$P < 0.05$, **$P < 0.01$, ***$P < 0.001$, n.s. not significant, $P > 0.05$).

**Supplementary figures**
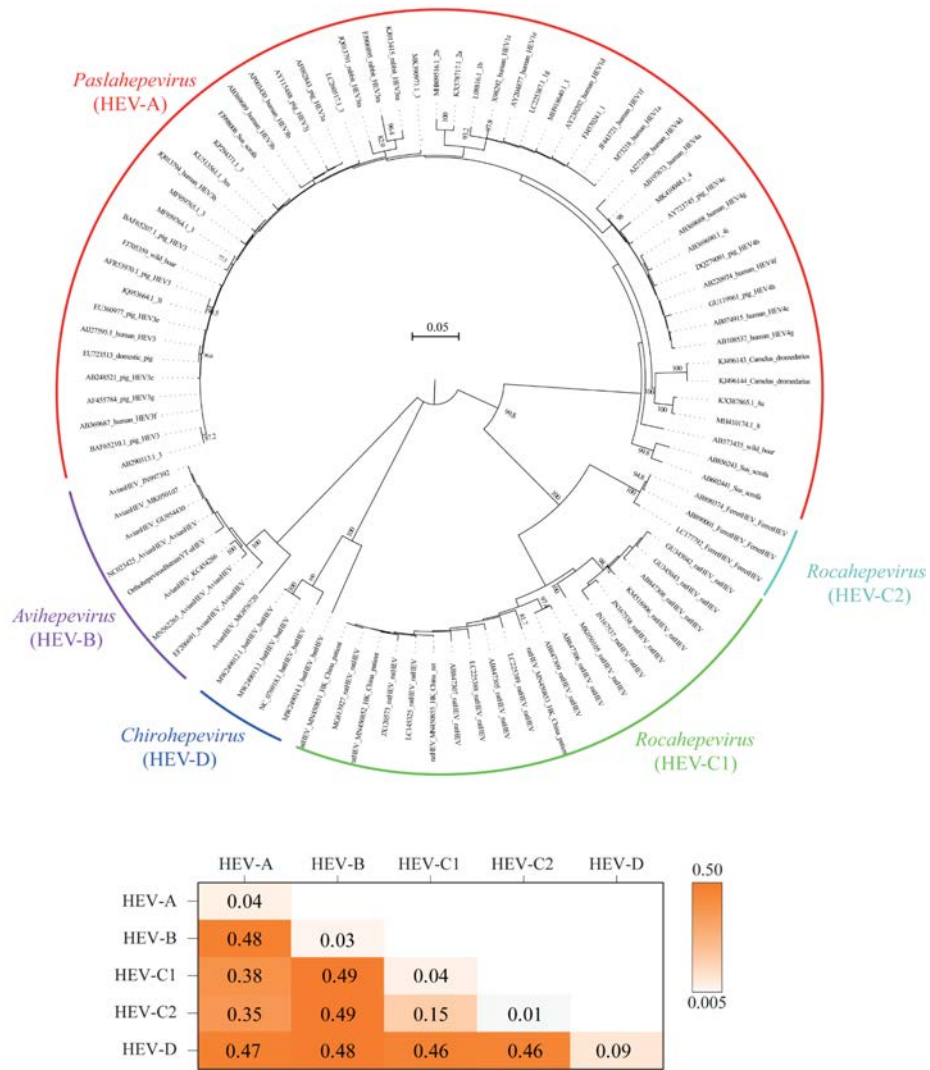


**Fig. S1.** The Neighbor-Joining tree was constructed based on the amino acid sequences of ORF2 protein of the reference HEV sequences (7, 8). The colors outside indicate HEV genera (A-D). The scale bar indicated the distances of ORF2 amino acid sequences. Branch support was calculated using 1000 replications, and only bootstrap values >70 were shown. The matrix below showed the mean pairwise genetic distance (p-distance) among ORF2 amino acid sequences of HEV A-D.

**Fig. S2. The consensus sequences of ORF2 (HEV-A to HEV-D) were illustrated.** The amino acid sequences of HEV ORF2 (A-D) were collected from NCBI (Table S1). The consensus sequences of HEV-A to HEV-D were generated. The red box indicates the regions of truncated ORF2 (named HEV-A ORF2$^T$, HEV-C1 ORF2$^T$, HEV-C2 ORF2$^T$, HEV-D ORF2$^T$, HEV-B ORF2$^T$) used to produce VLPs of HEV-A to HEV-D.
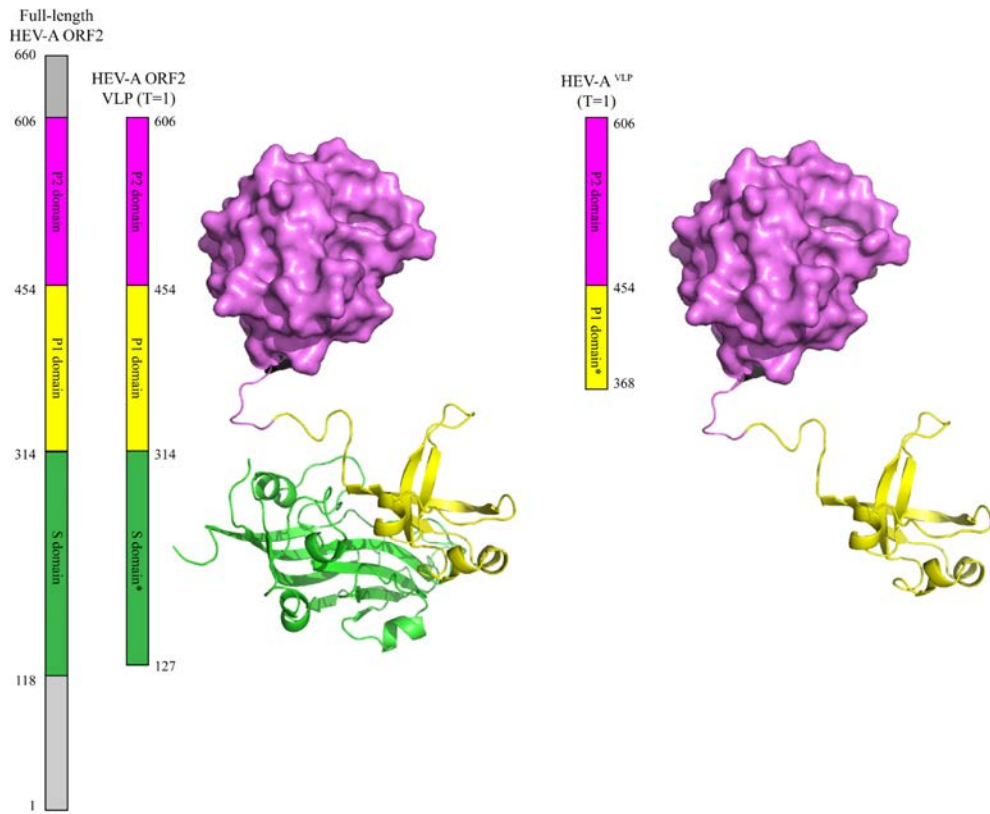
197

198 **Fig. S3. 3D structural model of the monomer of HEV-A ORF2^VLP**. The structure was

199 modeled by the Swiss-model. The P2, P1 and S domains are colored violet, yellow and green.

200 The HEV-A ORF2^VLP was assembled based on the multimerization of HEV-A ORF2^T, which

201 contained the full P2 domain (aa454-606) and partial P1 domain (aa368-453). The 3D structure

202 of HEV-A^VLP (T=1) was generated by the program PyMol.

203

204
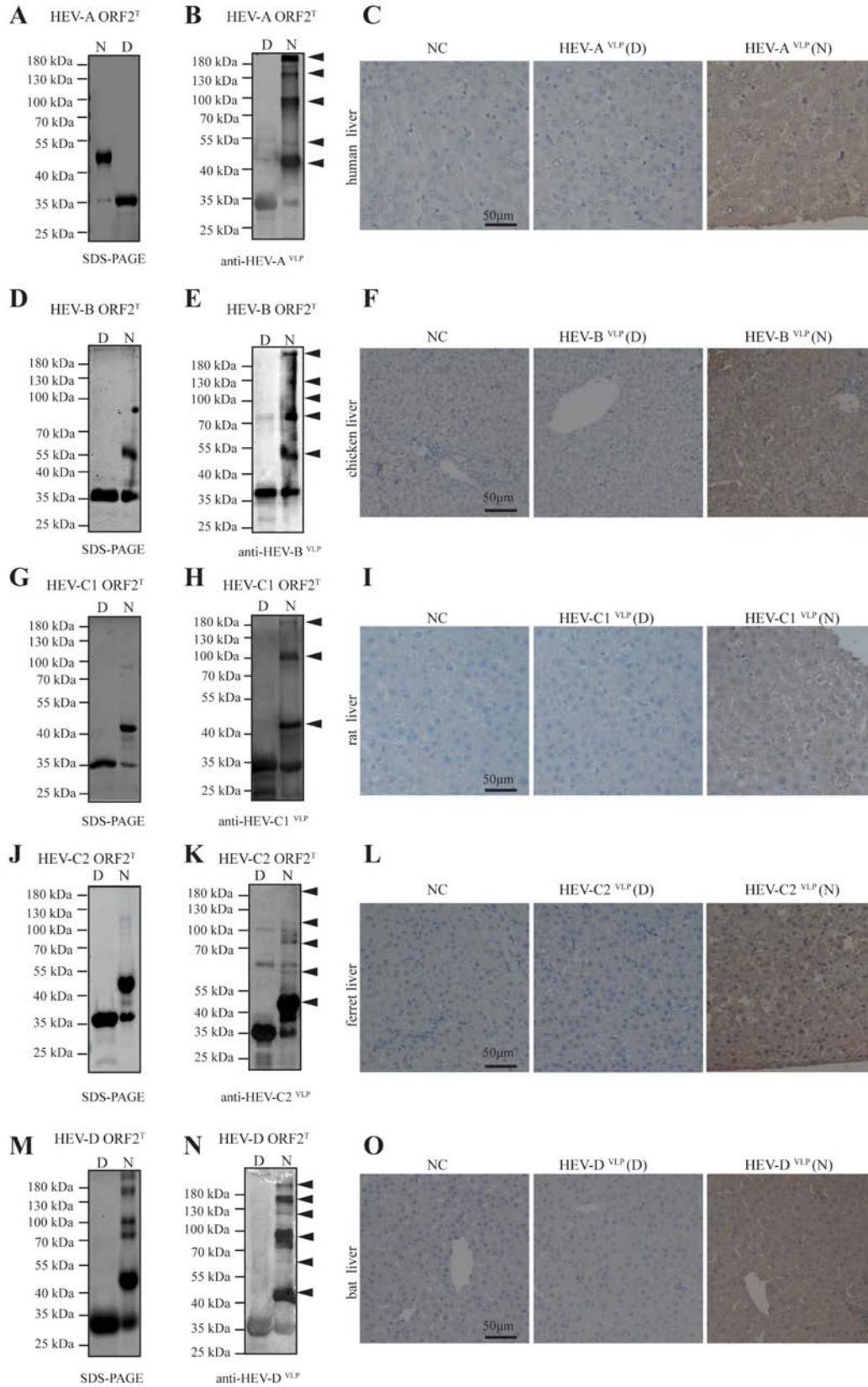
**Fig. S4. Generation and characterization of VLPs of HEV-A to HEV-D. (A, D, G, J, M)** C-

207 terminally his-tagged HEV-A ORF2$^T$ **(A)**, HEV-B ORF2$^T$ **(D)**, HEV-C1 ORF2$^T$ **(G)**, HEV-C2

208 ORF2$^T$ **(J)**, HEV-D ORF2$^T$ **(M)** were expressed in *E. coli* and purified. Non-denatured (N) and

209 denatured (D) protein samples were analyzed by SDS-PAGE. **(B, E, H, K, N)** C-terminally his-

210 tagged HEV-A ORF2$^T$ **(B)**, HEV-B ORF2$^T$ **(E)**, HEV-C1 ORF2$^T$ **(H)**, HEV-C2 ORF2$^T$ **(K)**,

211 HEV-D ORF2$^T$ **(N)** were expressed in *E. coli* and purified. Non-denatured (N) and denatured

212 (D) HEV-A ORF2$^T$ proteins were analyzed by western blots with rabbit antibodies against their

213 corresponding VLPs. The dimer and multimeric protein structures were indicated with black

214 arrows. **(C)** The binding capacity of non-denatured (N) and denatured (D) HEV-A$^{VLP}$ on human

215 liver tissue slides was detected by immunohistochemistry. **(F, I, L, O)** Same as (C) for detecting

216 the binding capacity of non-denatured and denatured HEV-B$^{VLP}$ (F), HEV-C1$^{VLP}$ (I), HEV-

217 C2$^{VLP}$ (L) and HEV-D$^{VLP}$ (O) on their cognate host liver tissue slides by immunohistochemistry.

218 The images presented are the representative of at least two independent experiments.

219

220
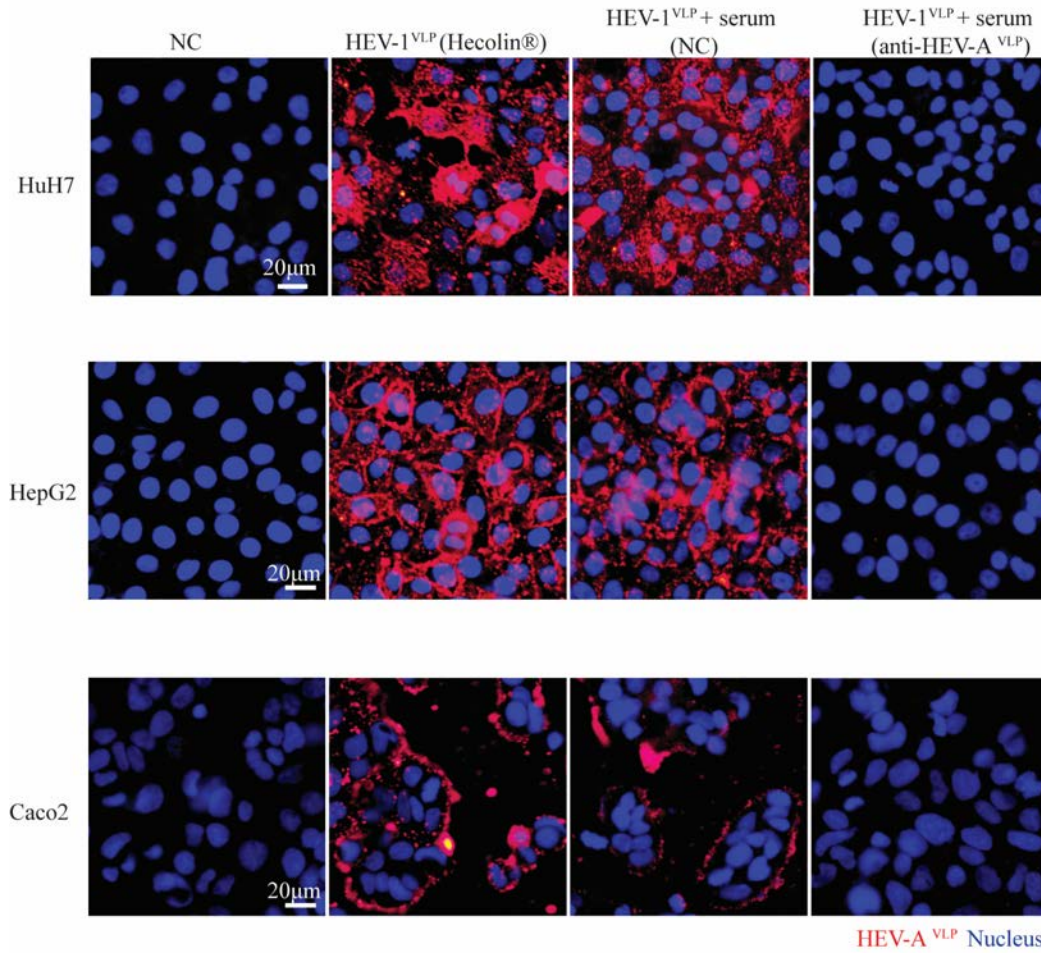
Fig. S5. Detection of cell binding ability of HEV-1$^{VLP}$. HEV-1$^{VLP}$ is the main component of HEV vaccine Hecolin®. HuH7, HepG2 and Caco2 cells were incubated with PBS (NC), HEV-1$^{VLP}$, HEV-1$^{VLP}$ + serum (NC, dilution 1:20), HEV-1$^{VLP}$ + serum (anti-HEV-C1$^{VLP}$, dilution 1:20). The binding capacity of HEV-1$^{VLP}$ was detected by immunofluorescence assay. The images presented are the representative of three independent experiments.

228
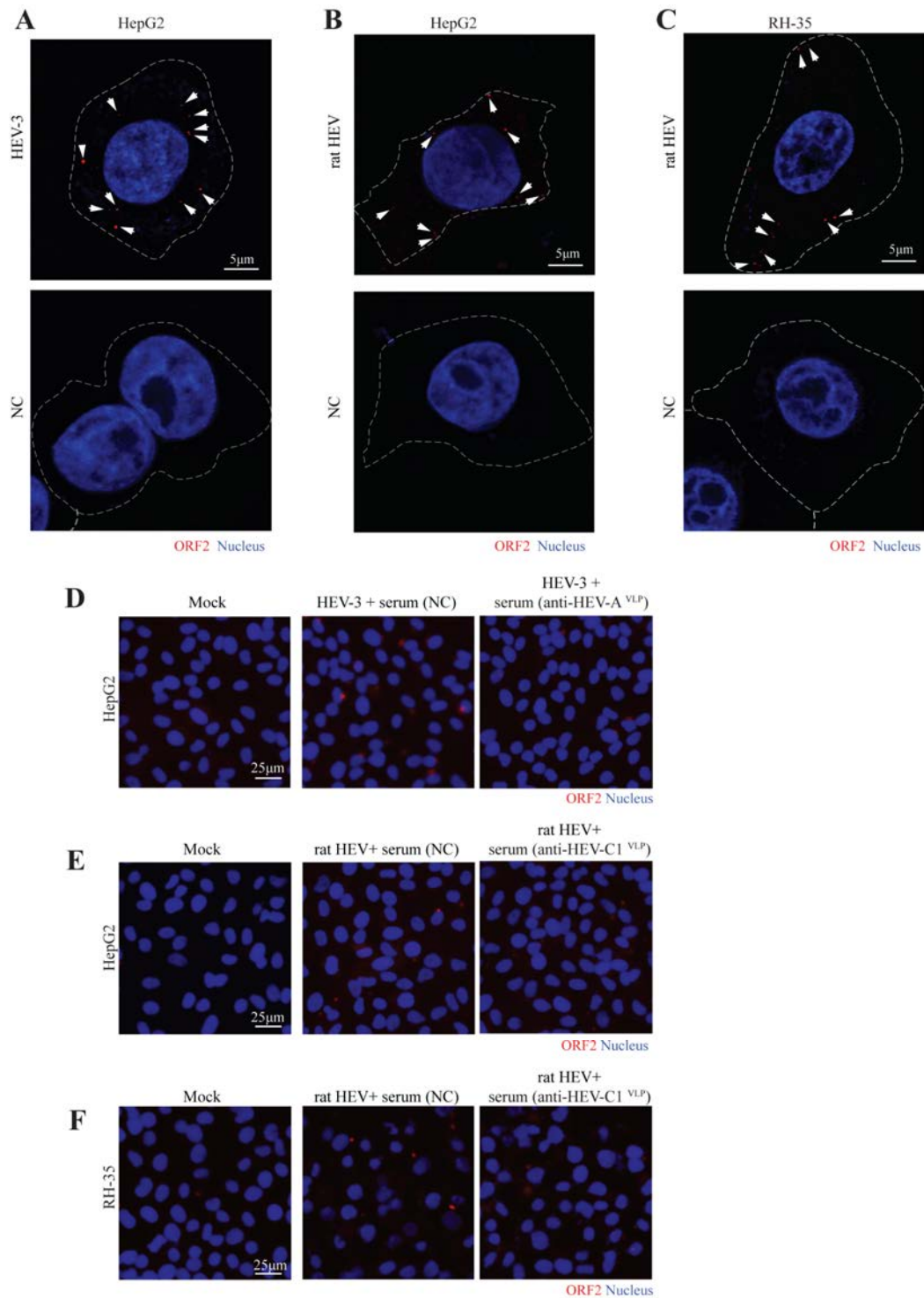
**Fig. S6. Detection of cell entry capability of HEV-C1$^{VLP}$ and infectious rat HEV particles.**

**(A)** HepG2 cells were inoculated with mock or HEV-3 virus ($1\times10^4$ copy numbers per cell) for 1h at 37℃. The entry potency of HEV-3 in HepG2 cells was detected by confocal immunofluorescence assay. Hoechst (blue) and ORF2 polyclonal antibodies were applied to

14

visualize nuclei and viral ORF2 protein. In addition, bright field microscopy channel was used

to determine outlines of adherent cells. Cell boundary was illustrated with white dash lines. The

images presented are the representative of three independent experiments. **(B)** Same as (A) for

detecting entry of rat HEV in HepG2 cells. **(C)** Same as (A) for detecting entry of rat HEV in

RH-35 cells. **(D)** HepG2 cells were inoculated with mock or human HEV-3 virus ($\sim3.3\times10^3$

copy number/cell) with rat serum (NC, dilution 1:20), or rat serum (anti-HEV-A$^{VLP}$, dilution

1:20) overnight, then washed with PBS extensively. ORF2 protein immunostaining (red) and

DAPI counterstaining (blue) was performed six days post inoculation. The images presented

are the representative of three independent experiments. **(E-F)** Same as (D) for the detection of

ORF2 positive cells post rat HEV ($\sim1.3\times10^3$ copy number per cell) inoculation in HepG2 or

RH-35 cells.
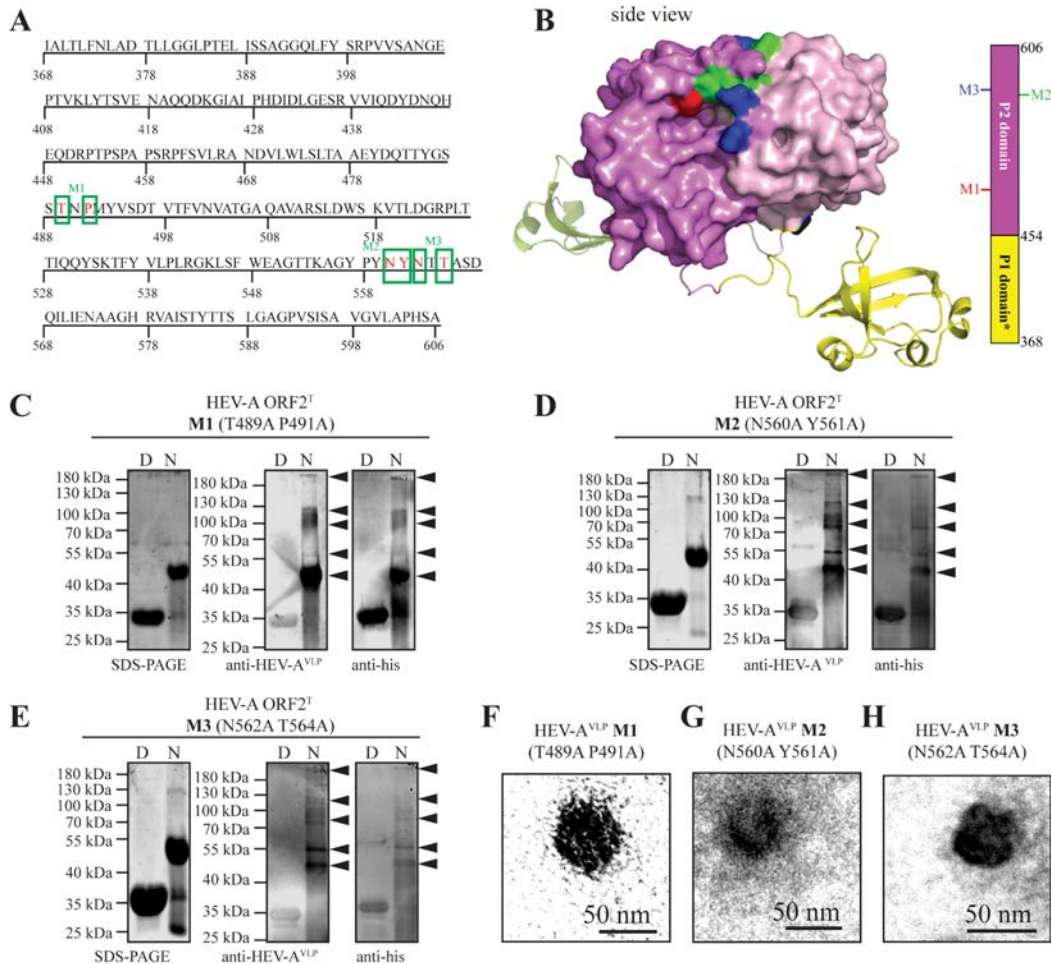
247 **Fig. S7. Generation and characterization of HEV-A$^{\text{VLP}}$ mutants. (A)** Amino acid sequences

248 of HEV-A ORF2$^{\text{T}}$. The mutant sites were labeled with red color. **(B)** Structural model of HEV-

249 A ORF2$^{\text{T}}$ dimer. The P2 (454-606) and truncated P1 (368-453) domains of the left side

250 monomer are colored violet and yellow, whereas the monomer on the right is light pink and

251 lemon. The mutant sites were depicted with red (M1), green (M2) and blue (M3). **(C)** C-

252 terminally his-tagged HEV-A ORF2$^{\text{T}}$ M1 was expressed in *Escherichia coli* BL21 strain and

253 purified. Non-denatured (N) and denatured (D) HEV-A ORF2$^{\text{T}}$ M1 were analyzed by SDS-

254 PAGE (left panel) and Western blots (middle panel: detected with rabbit anti-HEV-A$^{\text{VLP}}$

255 antibody, right panel: detected with anti-his antibody). The dimer and multimeric protein

256 structures were indicated with black arrow. **(D) and (E)** Same as (A) for the characterization of

257 HEV-A ORF2$^{\text{T}}$ M2 and HEV-A ORF2$^{\text{T}}$ M3 proteins. The images presented are the

258 representative of three independent experiments. **(F-H)** Analysis of self-assembled

259 recombinant HEV-A$^{\text{VLP}}$ M1, HEV-A$^{\text{VLP}}$ M2 and HEV-A$^{\text{VLP}}$ M3 by transmission electron

260 microscopy (TEM).

261



262

16
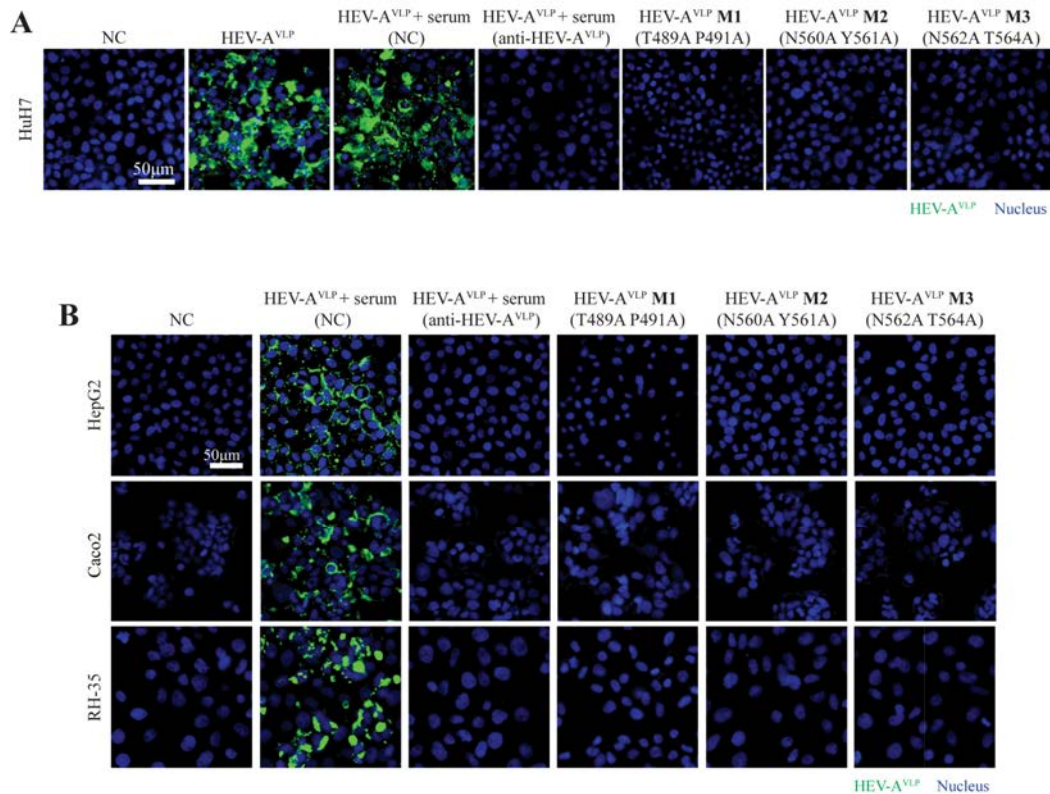
263 **Fig. S8 Characterization of the cell binding capability of HEV-A$^{VLP}$ mutants. (A)** The

264 binding capability of WT and mutant HEV-A$^{VLP}$ (M1-M3) to HuH7 cells was detected by

265 immunofluorescence assay. **(B)** The binding capability of the mutant HEV-A$^{VLP}$ (M1-M3) to

266 HepG2, Caco2 and RH-35 cells was detected by immunofluorescence assay.
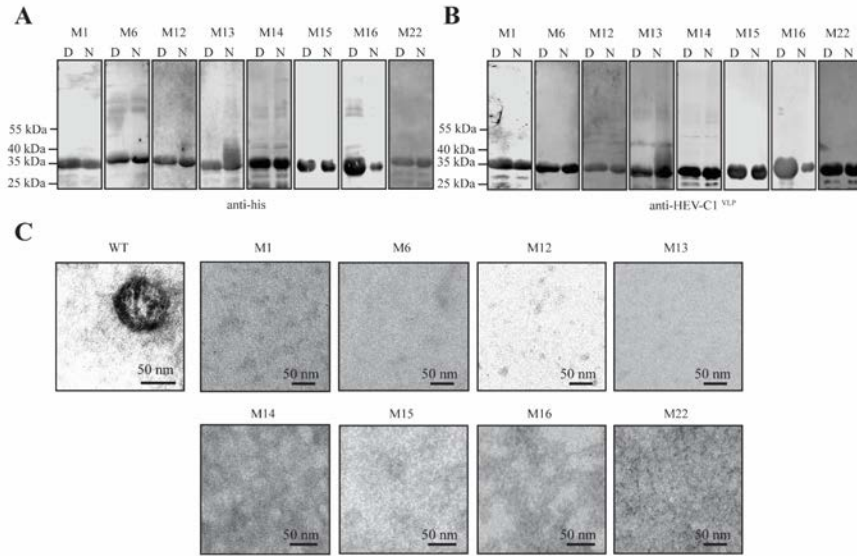


267

268 **Fig. S9. Identification of amino acid residues involved in HEV-C1$^{VLP}$ formation. (A-B)** C-

269 terminally his-tagged HEV-C1 ORF2$^{T}$ mutants (M1, M6, M12, M13, M14, M15, M16, M22)

270 were expressed and purified. Non-denatured (N) and denatured (D) HEV-C1 ORF2$^{T}$ mutants

271 were analyzed by western blots with anti-his antibody (A) or rabbit anti-HEV-C1$^{VLP}$ antibody

272 (B). No dimer or multimeric protein structures were observed. The images presented are the

273 representative of three independent experiments. **(C)** Electron microscopic analysis of WT and

274 mutant HEV-C1 ORF2$^{T}$.

275

276
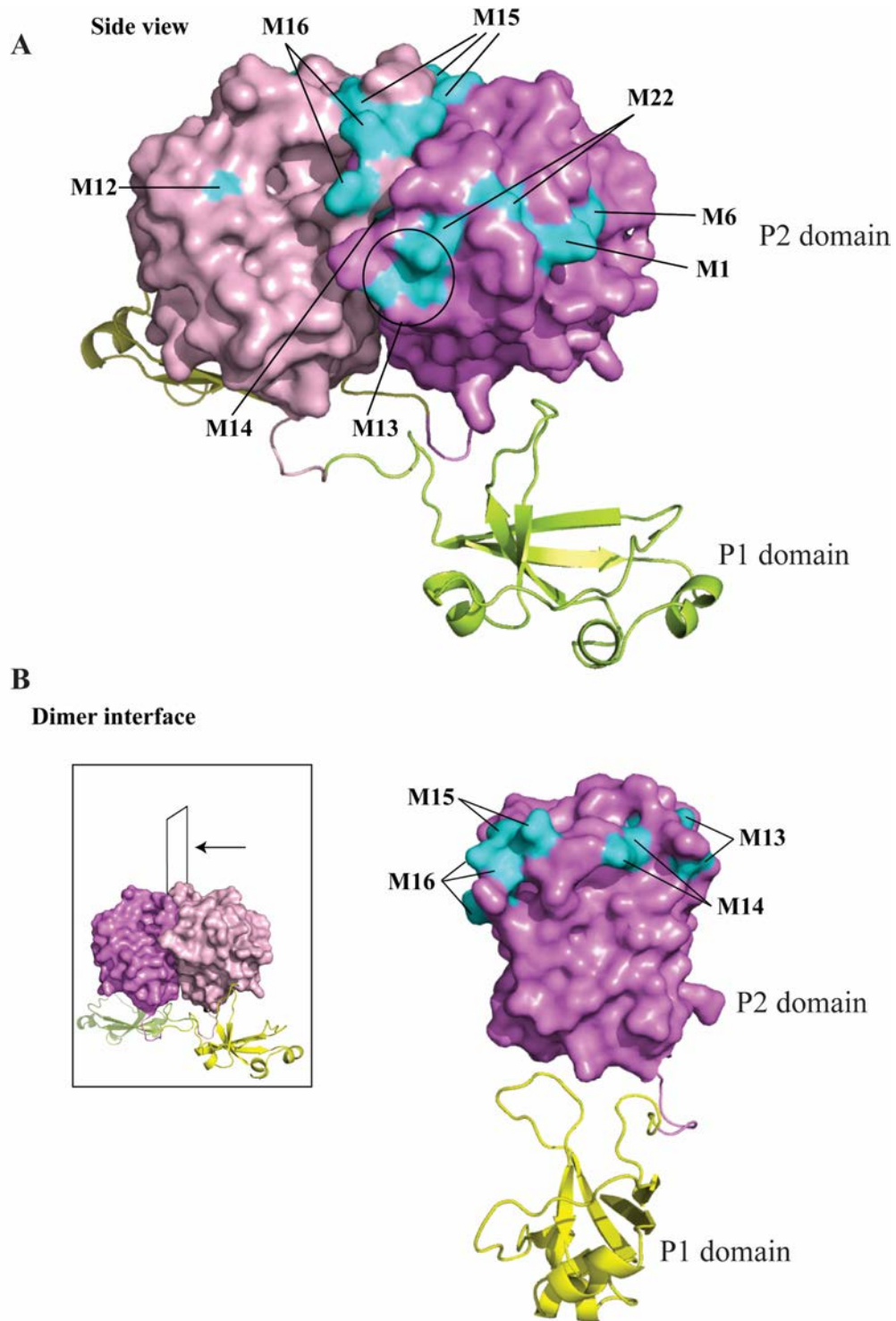
**Fig. S10. Illustration of amino acid residues involved in HEV-C1[VLP] formation.** Structural

model of HEV-C1 ORF2[T] dimer from side view **(A)** and dimer interface **(B)**. The substitutions

in the P2 domain essential for VLP formation were shown in cyan.
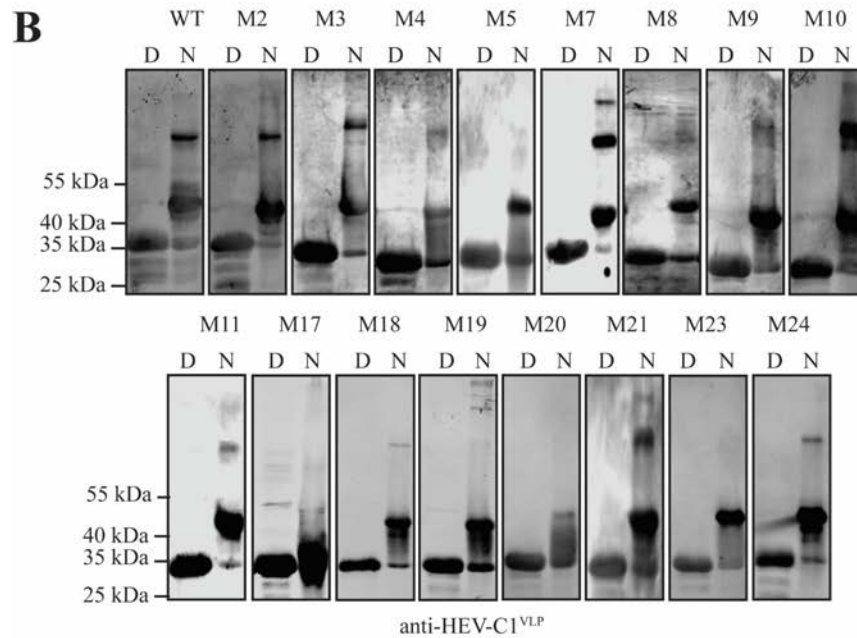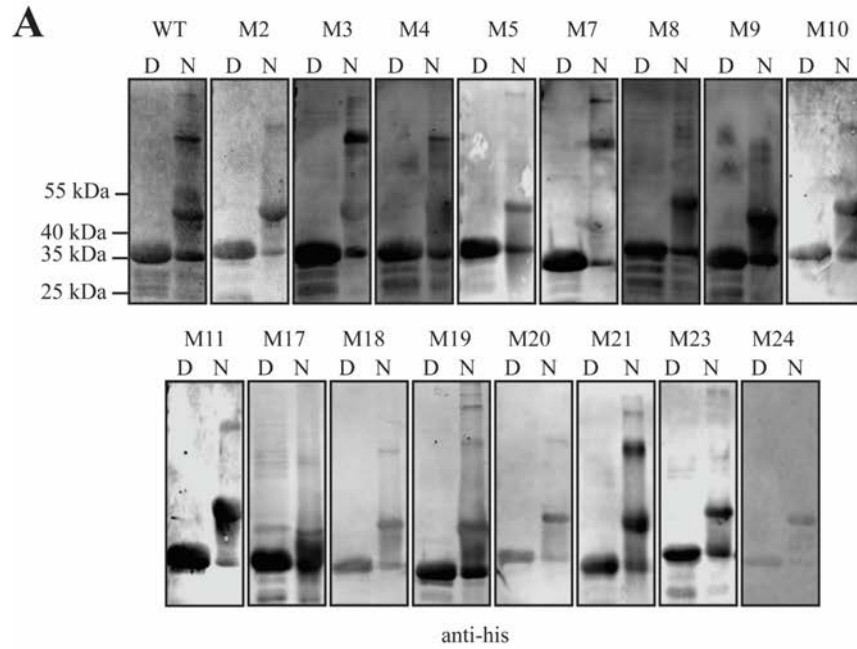
**Fig. S11. Identification of amino acid residues essential for HEV-C1$^{VLP}$ binding to target cells. (A)** C-terminally his-tagged HEV-C1 ORF2$^{T}$ mutants (M2, M3, M4, M5, M7, M8, M9, M10, M11, M17, M18, M19, M20, M21, M23, M24) were expressed and purified. Non-denatured (N) and denatured (D) mutants were analyzed by western blots with anti-his antibody

286 **(A)** or rabbit anti-HEV-C1$^{VLP}$ antibody **(B)**. The dimer or multimeric protein structures were

287 observed in all these mutants. The images presented are the representative of three independent

288 experiments.
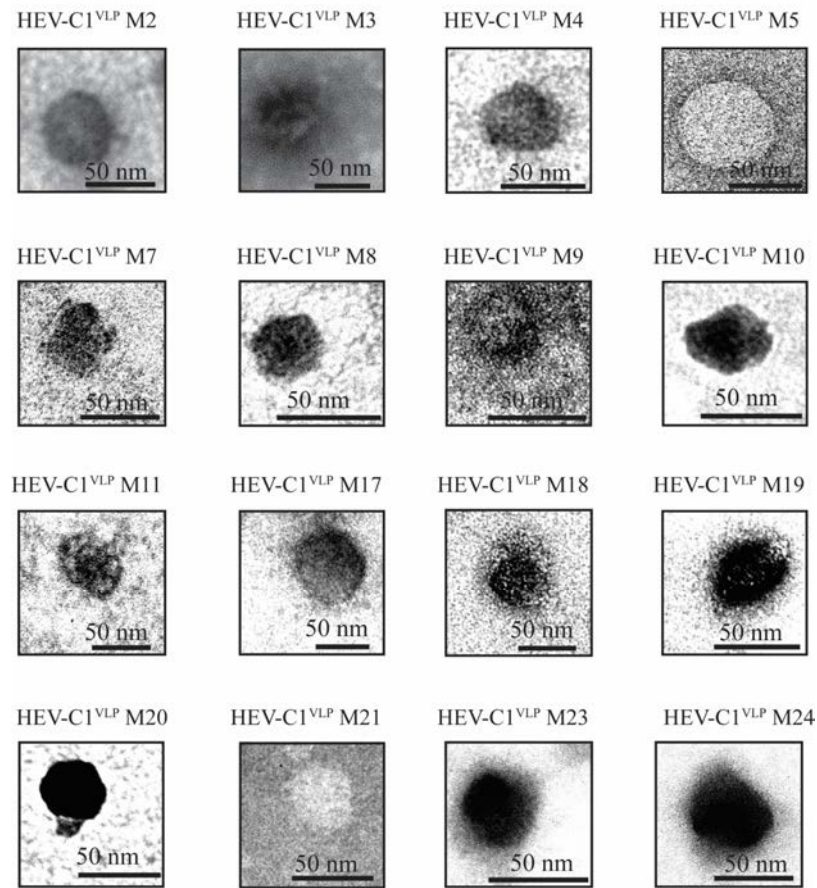


289

290 **Fig. S12. Electron microscopic images of HEV-C1$^{VLP}$ mutants.**

291

292
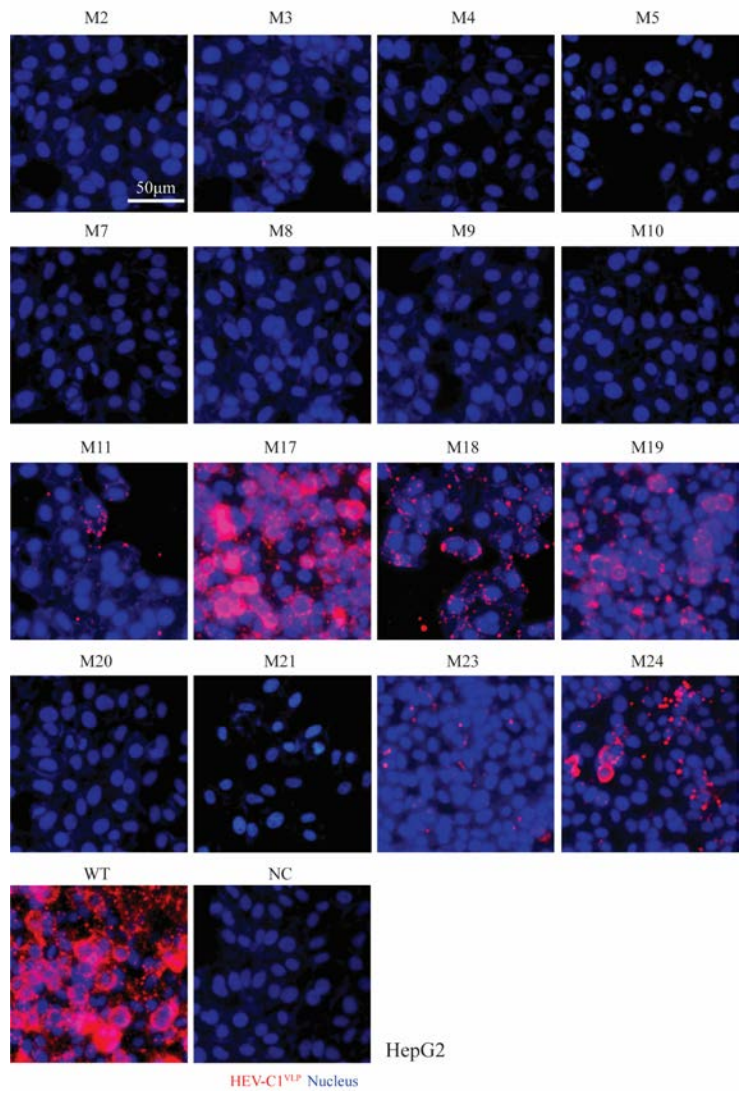
**Fig. S13. Binding capability of HEV-C1^{VLP} mutants to HepG2 cells was measured by**

**immunofluorescence assay.** The images presented are the representative of three independent

experiments.
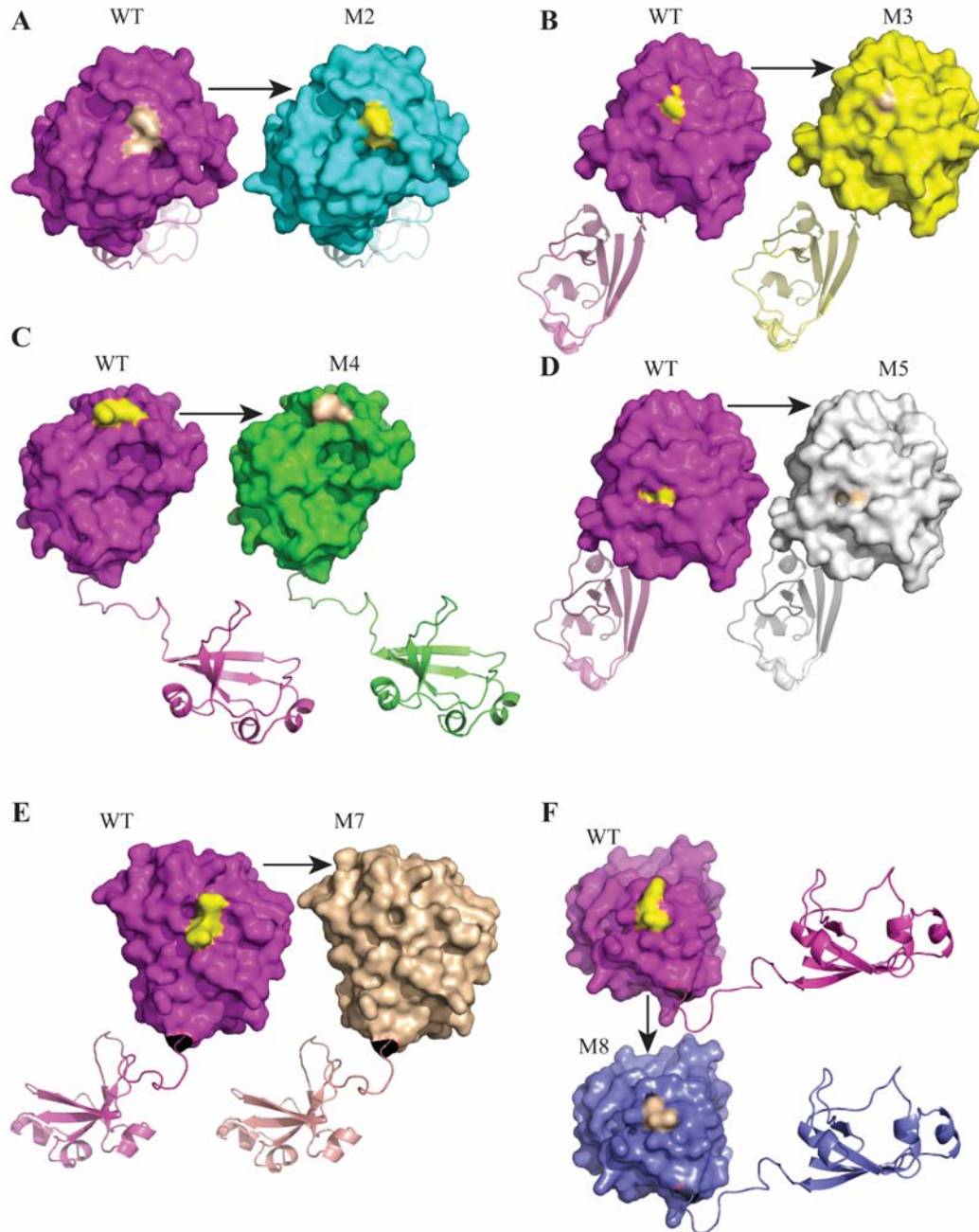
**Fig. S14. Structural modeling of wild type and mutant HEV-C1 ORF2$^T$ monomer.** For HEV-C1 ORF2T (M2-M8), conformational changes between wild-type and its mutant were analyzed. Amino acid residues essential for binding to susceptible cells were highlighted on the wild-type monomer. In parallel, their corresponding mutant sites were also indicated on each mutant monomer.

22

303
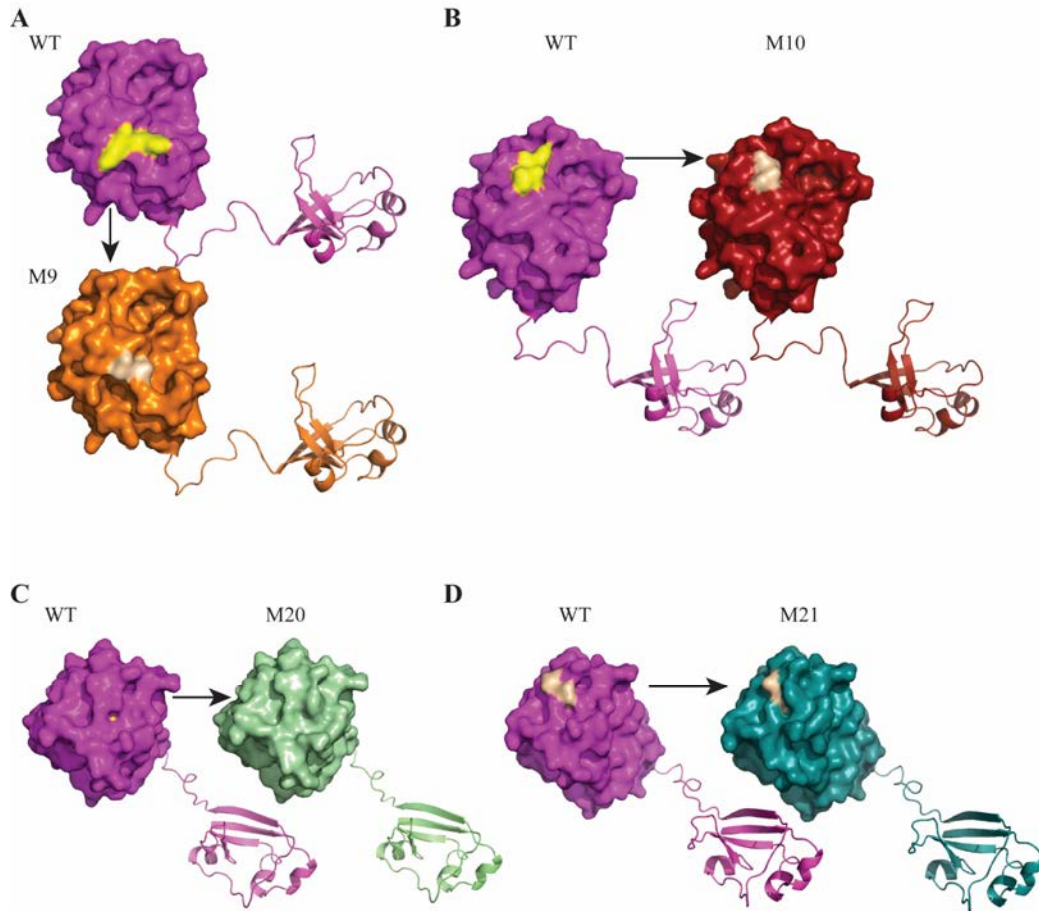
**Fig. S15. Structural modeling of wild type and mutant HEV-C1 ORF2$^T$ monomer.** For
HEV-C1 ORF2T (M9, M10, M20, M21), conformational changes between wild-type and its
mutant were analyzed. Amino acid residues essential for binding to susceptible cells were
highlighted on the wild-type monomer. In parallel, their corresponding mutant sites were also
indicated on each mutant monomer.
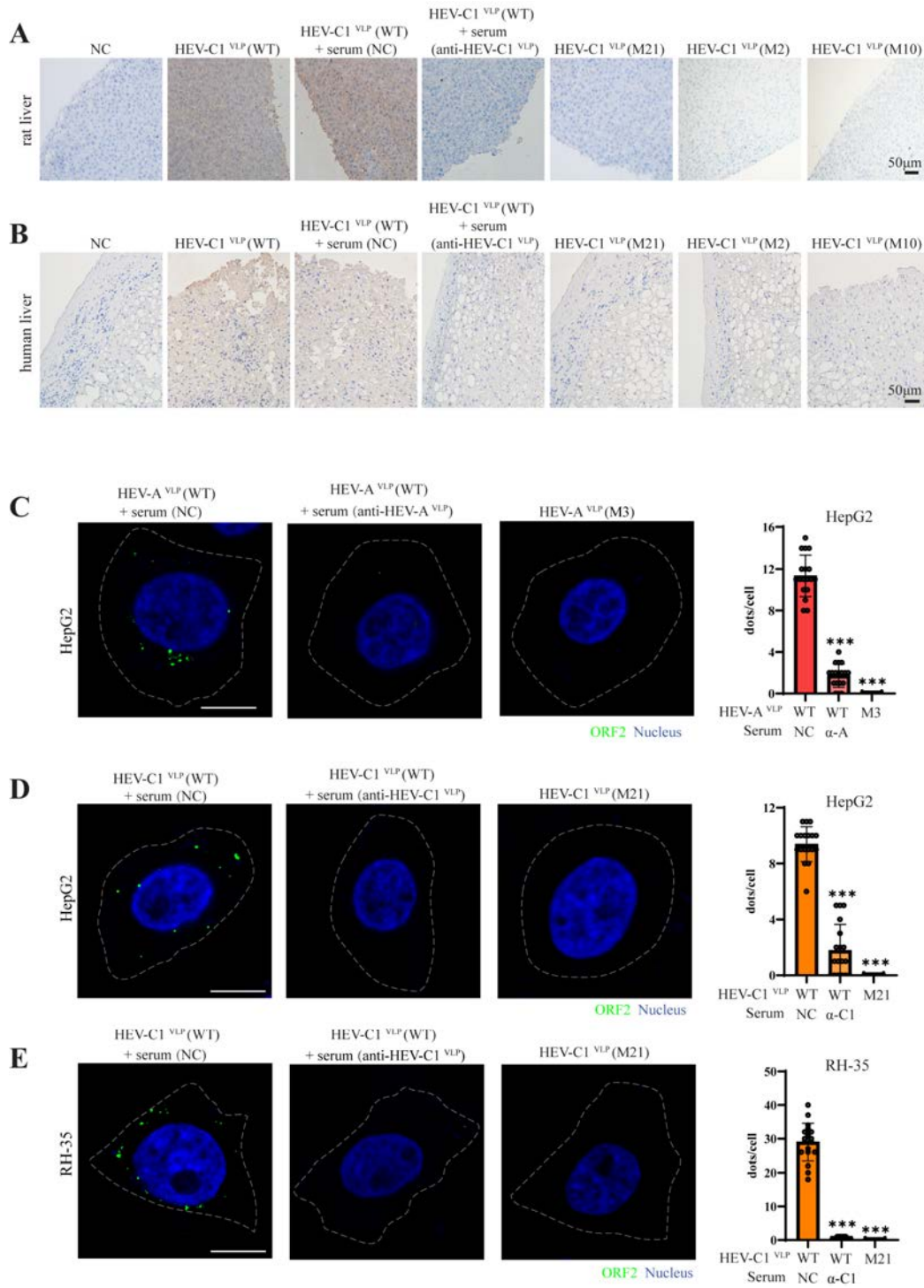
**Fig. S16. Detection of the binding and entry specificity of HEV-C1$^{VLP}$.** HEV-C1$^{VLP}$ was

preincubated with rat serum (NC, negative control, dilution 1:20) or rat serum (anti-HEV-C1$^{VLP}$,

dilution 1:20) for 45 mins at room temperature. **(A)** rat liver or **(B)** human liver tissue slides

315      were incubated with PBS (NC), HEV-C1$^{VLP}$ (WT), HEV-C1$^{VLP}$ (WT)+ rat serum (NC), HEV-

316      C1$^{VLP}$ (WT)+ rat serum (anti-HEV-C1$^{VLP}$), HEV-C1$^{VLP}$ (M21), HEV-C1$^{VLP}$ (M2) or HEV-C1$^{VLP}$

317      (M10) overnight at 4 ° C. The binding specificity of VLPs was detected by

318      immunohistochemistry. The images presented are the representative of three independent

319      experiments. **(C)** HepG2 cells were inoculated with the same amounts of HEV-A$^{VLP}$ (WT) + rat

320      serum (NC), HEV-A$^{VLP}$ (WT) + rat serum (anti-HEV-A$^{VLP}$), or the same amounts of HEV-A$^{VLP}$

321      (M3). Their entry capability towards HepG2 cells was detected by confocal

322      immunofluorescence assay. Bright field microscopy channel was used to determine outlines of

323      adherent cells. Cell boundary was illustrated with white dash lines. The intracellular positive

324      fluorescent dots were counted and quantified based on three independent experiments **(D and**

325      **E)** Same as (C) for detecting the entry capability of HEV-C1$^{VLP}$ (WT) and HEV-C1$^{VLP}$ (M21)

326      in HepG2 (D) and RH-35 (E) cells.
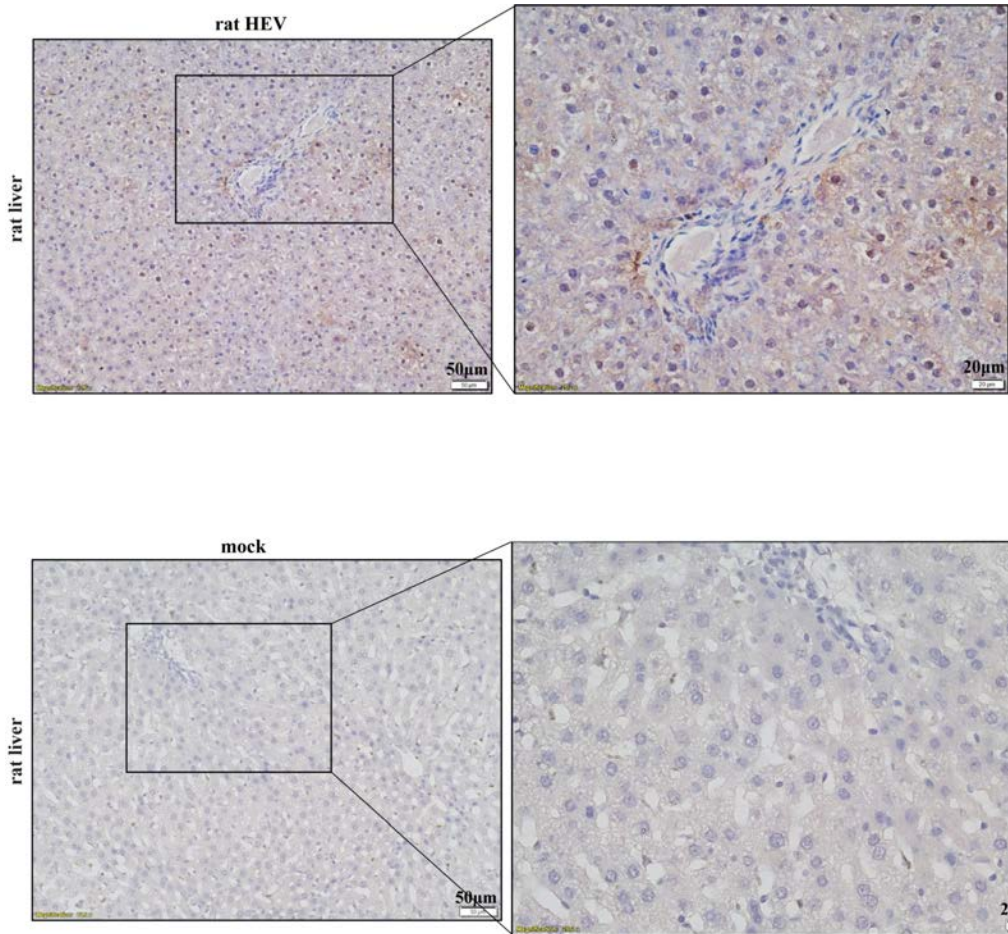
327
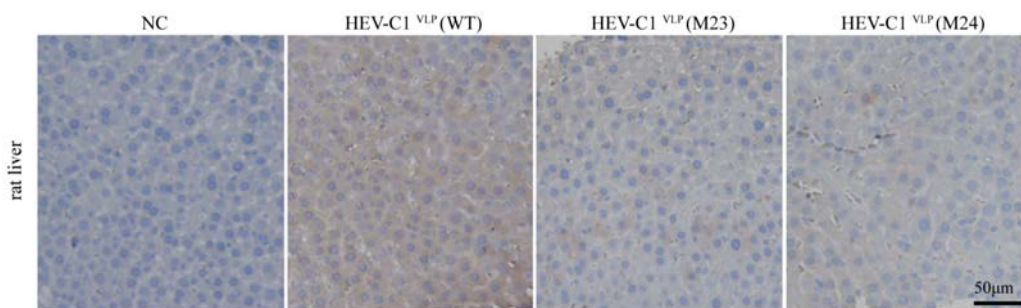


328

329

330      **Fig. S17. The binding capability of wild type and mutant versions (M23 and M24) of HEV-**

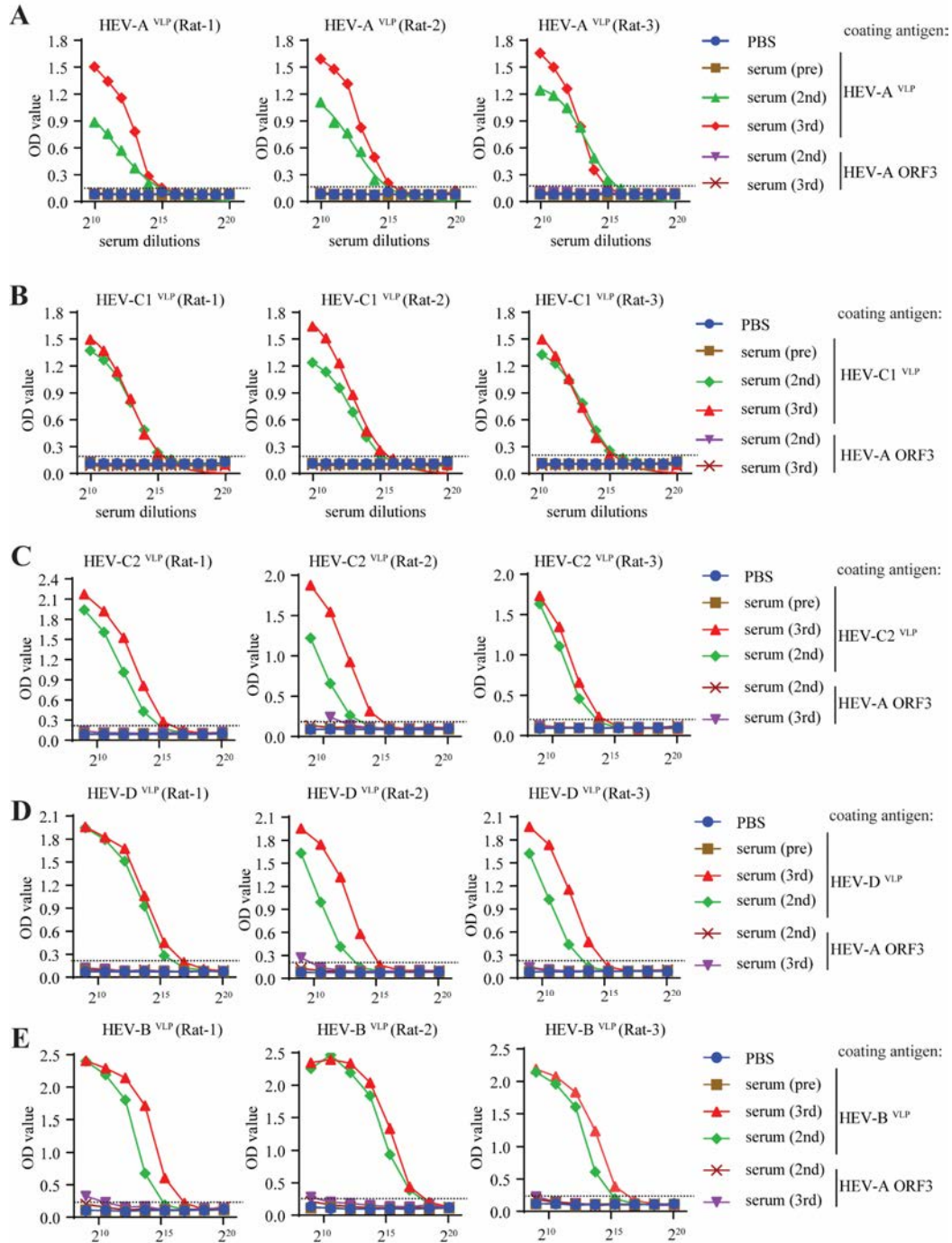331      **C1$^{VLP}$ was detected by immunohistochemistry.**

332

333

334

335

**Fig. S18. The liver tissues were collected from rat HEV infected rats or mock infected rats at day 28 and subjected to immunohistochemistry analysis of rat HEV ORF2 protein.**

336

337

338

**Fig. S19. The immunogenicity of five different VLPs was determined by ELISA. (A)** Three rats were immunized with HEV-A$^{VLP}$ at two-week intervals. Rat sera were collected before immunization or after the 2$^{nd}$ and 3$^{rd}$ immunizations. Flat-bottomed 96-well polystyrene microplates were coated with 200 ng/well of HEV-A$^{VLP}$ or his tagged HEV-A ORF3. The plates were incubated with the serially diluted rat serum. The IgG antibody titers were measured by

ELISA. Dotted lines indicate the cut-off value. **(B-E)** Same as (A) for measuring the

immunogenicity of HEV-C1$^{VLP}$ (B), HEV-C2$^{VLP}$ (C), HEV-D$^{VLP}$ (D), and HEV-B$^{VLP}$ (E).
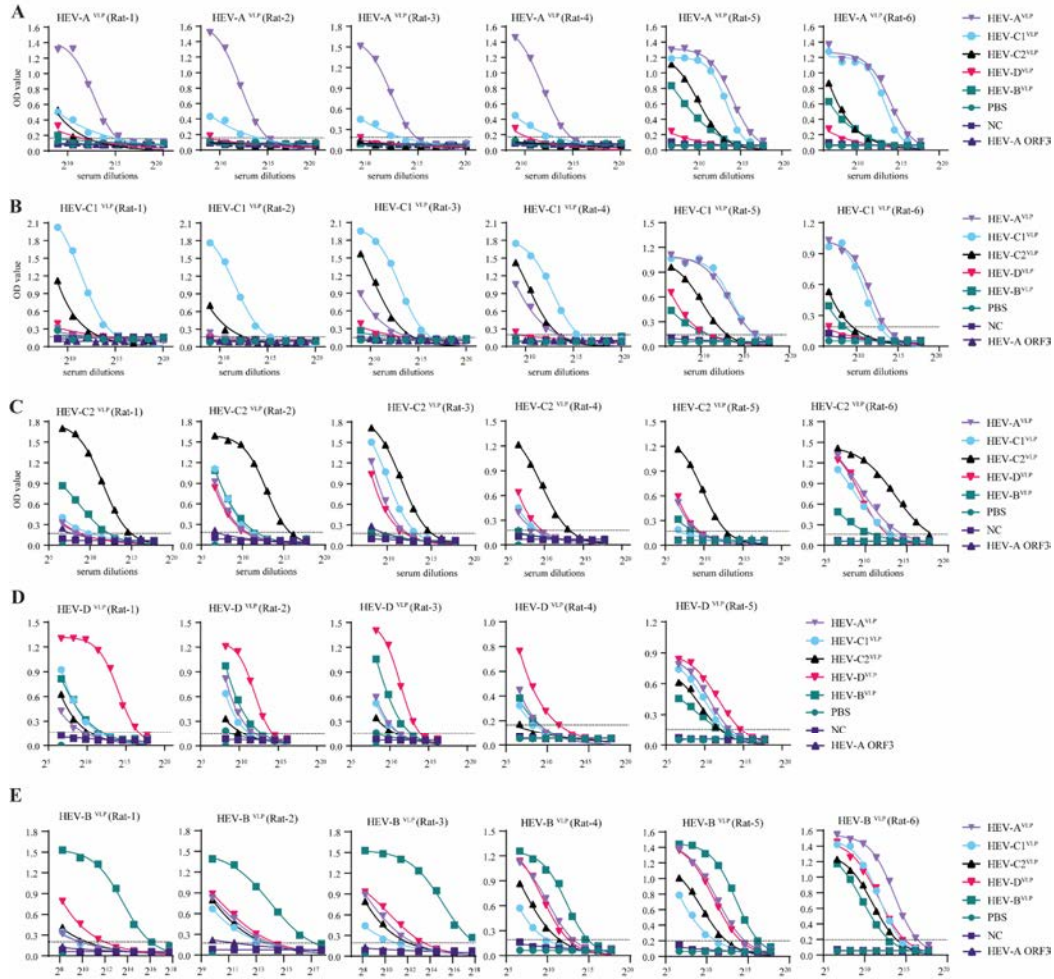


**Fig. S20. Measurement of antigenic cross-reactivity among HEV-A$^{VLP}$, HEV-C1$^{VLP}$, HEV-C2$^{VLP}$, HEV-D$^{VLP}$ and HEV-B$^{VLP}$ based on rat sera. (A)** Rats were immunized with HEV-A$^{VLP}$ at two-week intervals. Rat serum was collected after the 3$^{rd}$ immunization. Flat-bottomed 96-well polystyrene microplates were coated with 200 ng/well of HEV-A$^{VLP}$, HEV-C1$^{VLP}$, HEV-C2$^{VLP}$, HEV-D$^{VLP}$, HEV-B$^{VLP}$ or his tagged HEV-A ORF3. The plates were incubated with the serially diluted rat serum. The reactivity of anti-HEV-A$^{VLP}$ IgG to its homologous antigen HEV-A$^{VLP}$ and heterologous antigens was examined by ELISA. Dotted lines indicate the cut-off value. **(B-E)** Same as (A) for presenting HEV-C1$^{VLP}$ (B), HEV-C2$^{VLP}$ (C), HEV-B$^{VLP}$ (D) and HEV-D$^{VLP}$ (E).
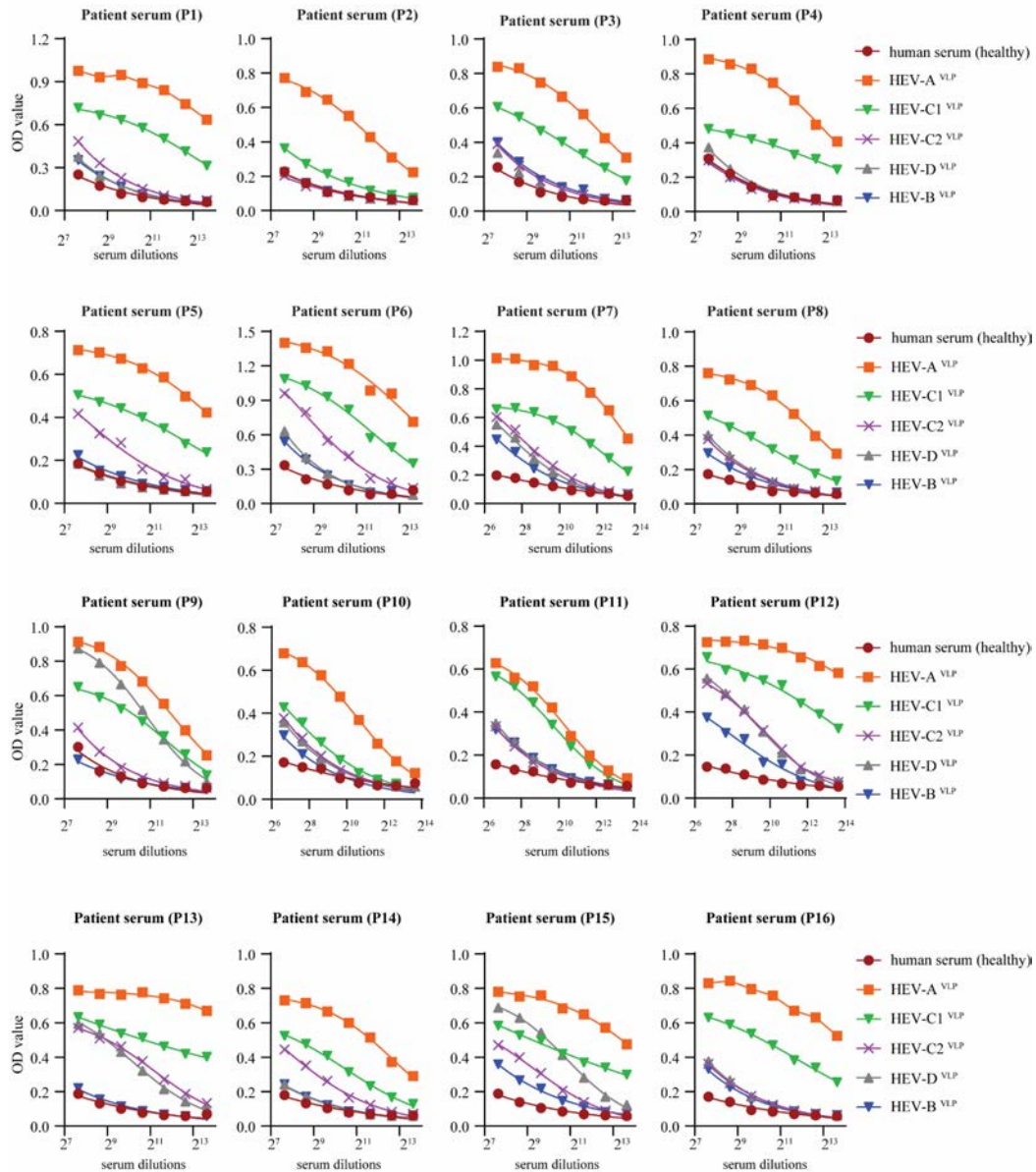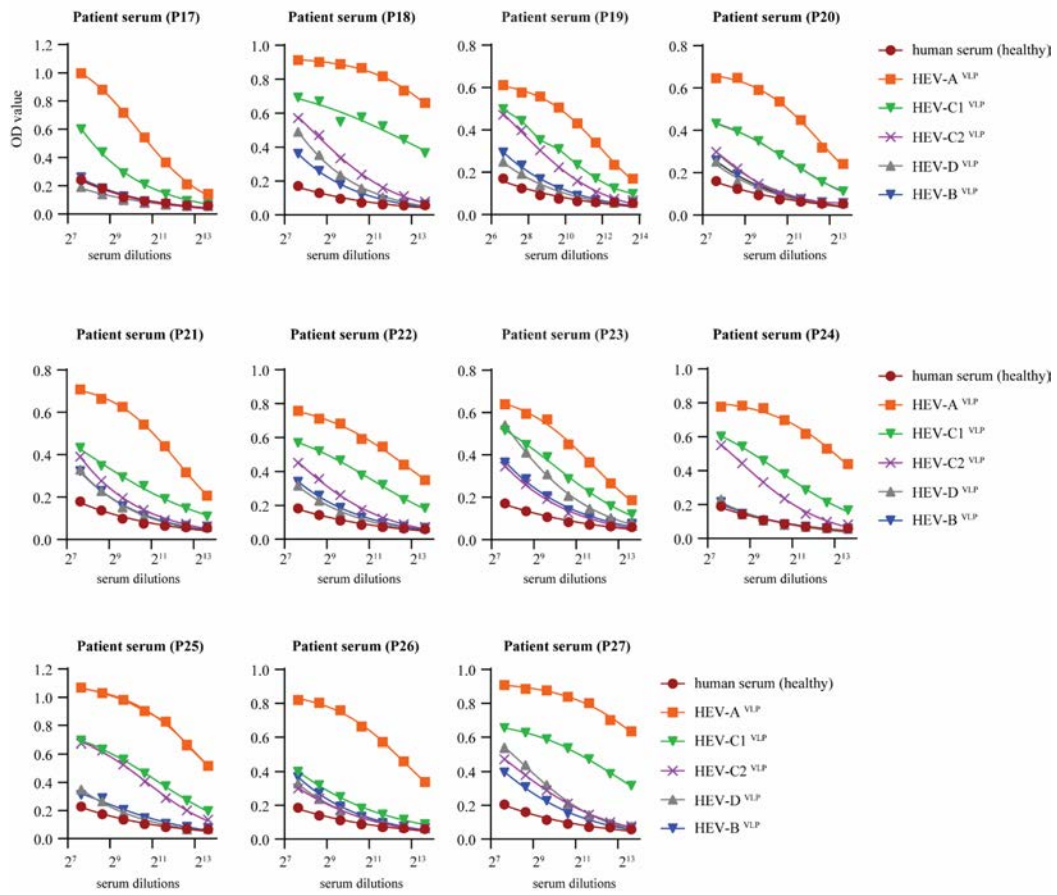
**Fig. S21. Measurement of antigenic cross-reactivity among HEV-A$^{VLP}$, HEV-C1$^{VLP}$, HEV-C2$^{VLP}$, HEV-D$^{VLP}$ and HEV-B$^{VLP}$ based on HEV-A patient sera (P1-P16).** HEV-A infected patient serum samples were collected. Flat-bottomed 96-well polystyrene microplates were coated with 200 ng/well of HEV-A$^{VLP}$, HEV-C1$^{VLP}$, HEV-C2$^{VLP}$, HEV-D$^{VLP}$, HEV-B$^{VLP}$. The plates were incubated with the serially diluted patient serum. The reactivity of anti-HEV-A$^{VLP}$ IgM to its homologous antigen HEV-A$^{VLP}$ and heterologous antigens was examined by ELISA.

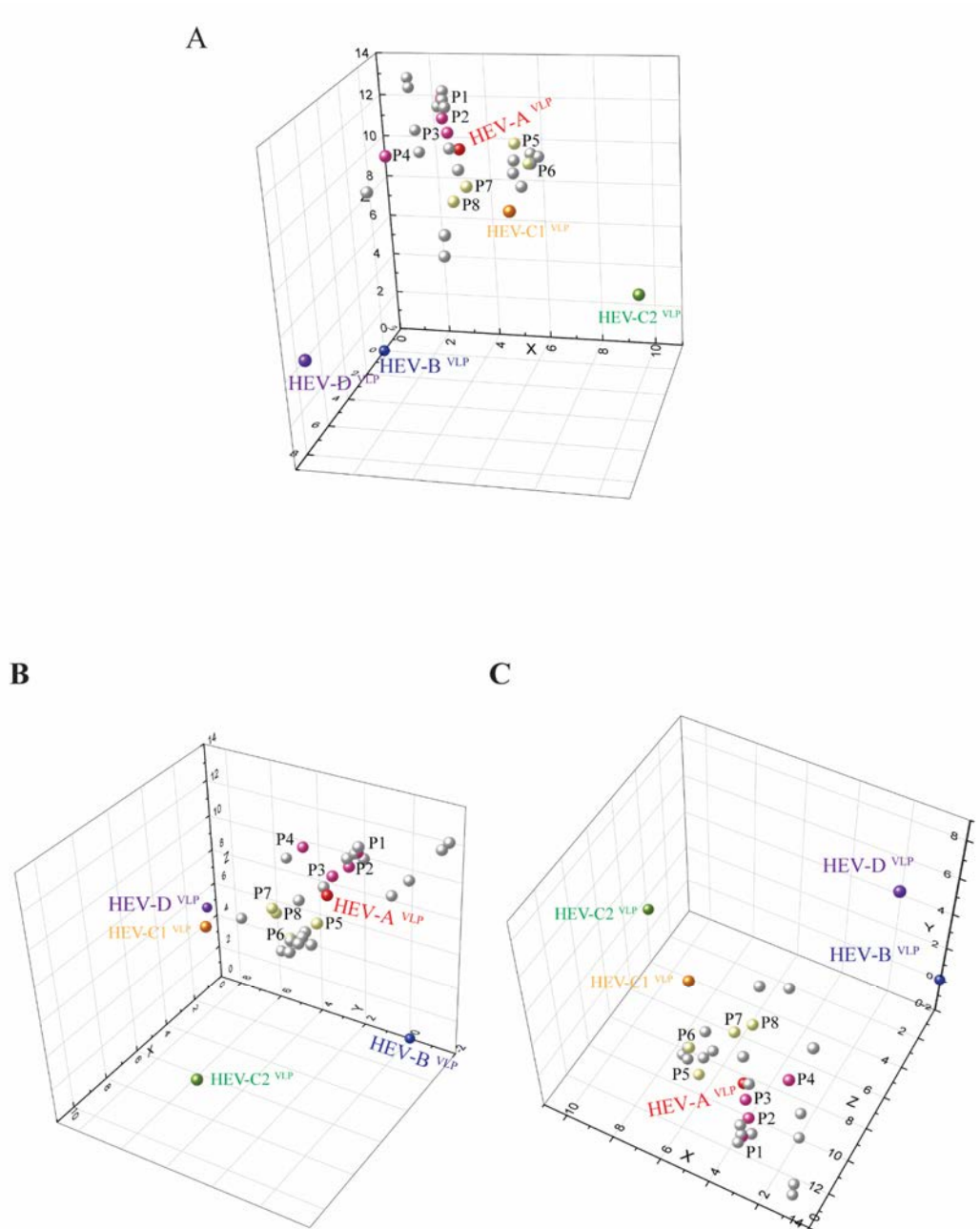Fig. S22. Measurement of antigenic cross-reactivity among HEV-A$^{VLP}$, HEV-C1$^{VLP}$, HEV-C2$^{VLP}$, HEV-D$^{VLP}$ and HEV-B$^{VLP}$ based on HEV-A patient sera (P17-P27).

371

**Fig. S23. Mapping the antigenic cartography of different HEV species with HEV-A patient sera. (A-C)** Three-dimensional cartographic projection reveals the antigenic relationships of different genera of HEV VLPs with HEV-A infected patient sera. Cluster positions from key angles (left, right, top) are displayed. One unit of antigenic distance denotes a twofold difference in sera titers. The purple, blue, green, orange and red spheres represent HEV-D$^{VLP}$, HEV-B$^{VLP}$, HEV-C2$^{VLP}$, HEV-C1$^{VLP}$ and HEV-A$^{VLP}$, respectively. The grey, light green and light purple spheres illustrate the HEV-infected patient sera. Patient sera (P1-P4) of cluster 1

were indicated with light purple spheres, and P5-P8 of cluster 2 were represented with light

green spheres.

381



382
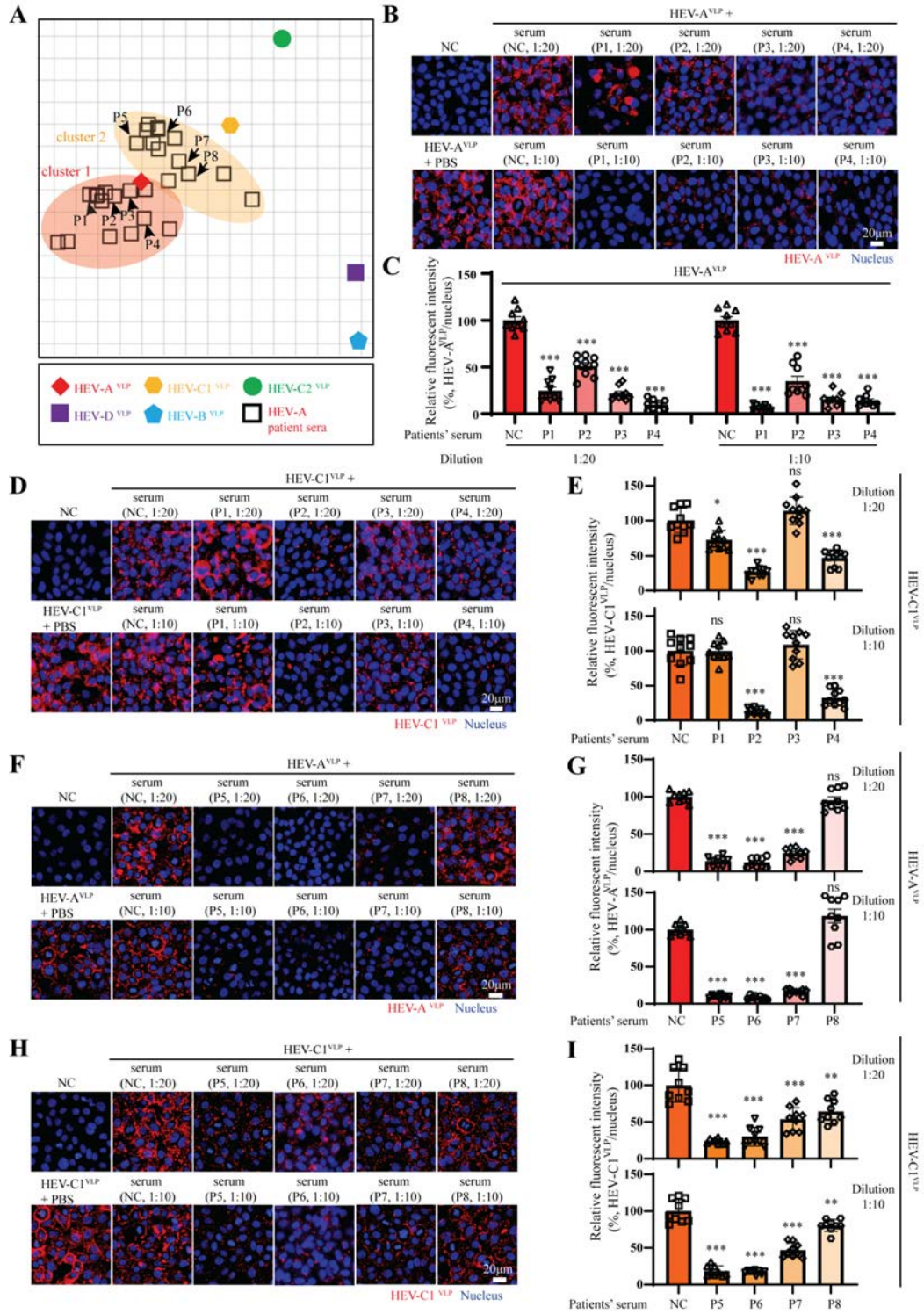
32

383 **Fig. S24. HEV-A patient sera exhibit partial cross-protection against the cell binding of**

384 **HEV-C1$^{VLP}$. (A)** Two-dimensional antigenic map of HEV-A$^{VLP}$, HEV-C1$^{VLP}$, HEV-C2$^{VLP}$,

385 HEV-B$^{VLP}$ and HEV-D$^{VLP}$ with HEV-A patient sera. The vertical and horizontal axes both

386 represent antigenic distance. One unit of antigenic distance denotes a two-fold difference in

387 sera titers. The red solid diamond, orange hexagon, green circle, purple square and blue

388 pentagon represent HEV-A$^{VLP}$, HEV-C1$^{VLP}$, HEV-C2$^{VLP}$, HEV-B$^{VLP}$ and HEV-D$^{VLP}$

389 respectively, whereas the hollow squares correspond patient sera collected from 27 HEV-A

390 infected individuals. Patient sera 1-8 (P1-P8) were indicated with black arrows. **(B and C)**

391 Human serum samples were collected from healthy volunteers or patients diagnosed and

392 hospitalized with acute HEV infection. The inhibitory efficacy of patient sera (P1-P4, cluster

393 1) against the binding of HEV-A$^{VLP}$ to HepG2 cells was measured by immunofluorescence

394 assay. The relative fluorescent intensity was quantified by ImageJ software based on three

395 independent experiments. **(D and E)** Same as (B and C) for detecting the inhibitory efficacy of

396 patient sera (P1-P4, cluster 1) against the binding of HEV-C1$^{VLP}$ to the cell membrane. **(F and**

397 **G)** Same as (B and C) for detecting the inhibitory efficacy of patient sera (P5-P8, cluster 2)

398 against the binding of HEV-A$^{VLP}$ to the cell membrane. **(H and I)** Same as (F and G) for

399 detecting the inhibitory efficacy of patient sera (P5-P8, cluster 2) against the binding of HEV-

400 C1$^{VLP}$ to the cell membrane.

401
402
403
404

33

405
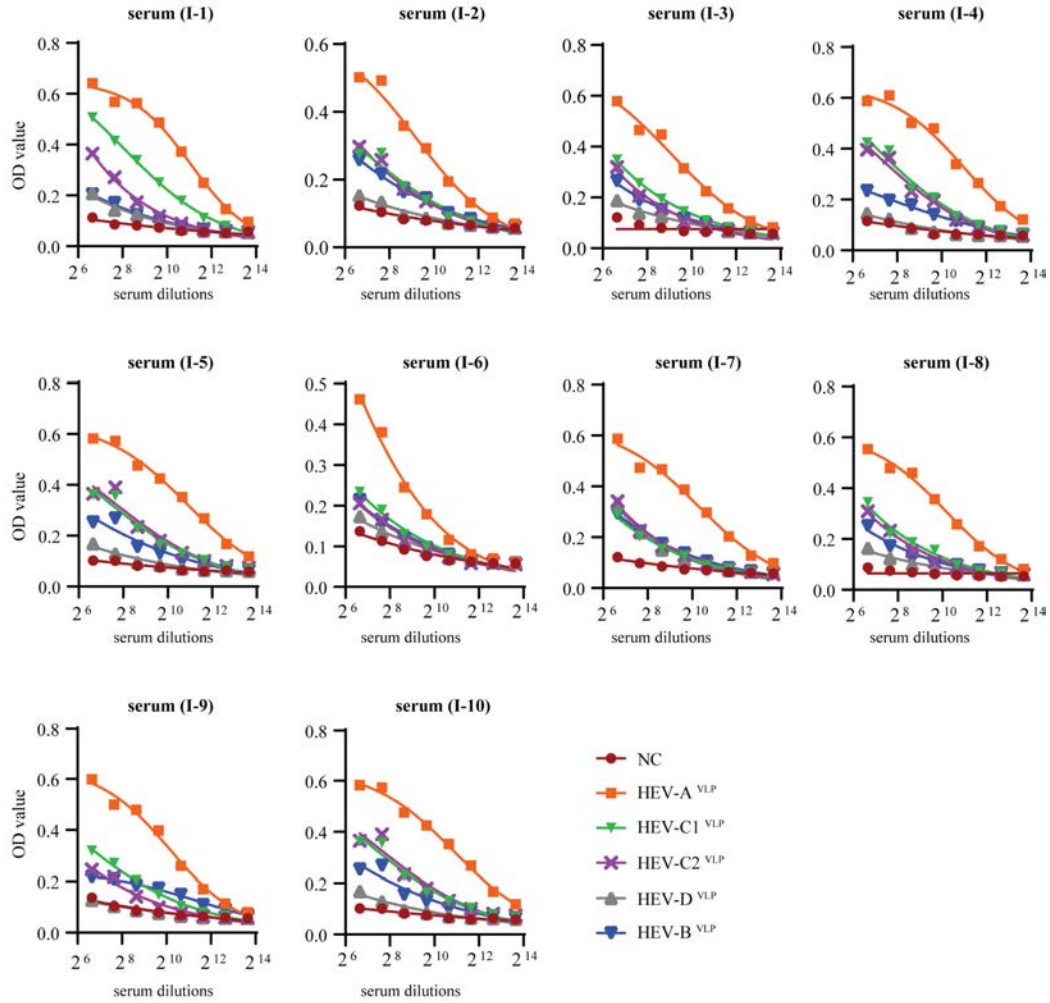
**Fig. S25. Measurement of antigenic cross-reactivity among HEV-A$^{VLP}$, HEV-C1$^{VLP}$, HEV-C2$^{VLP}$, HEV-D$^{VLP}$ and HEV-B$^{VLP}$ based on Hecolin immunized human sera.** Serum samples of ten individuals who completed Hecolin immunization were collected. Flat-bottomed 96-well polystyrene microplates were coated with 200 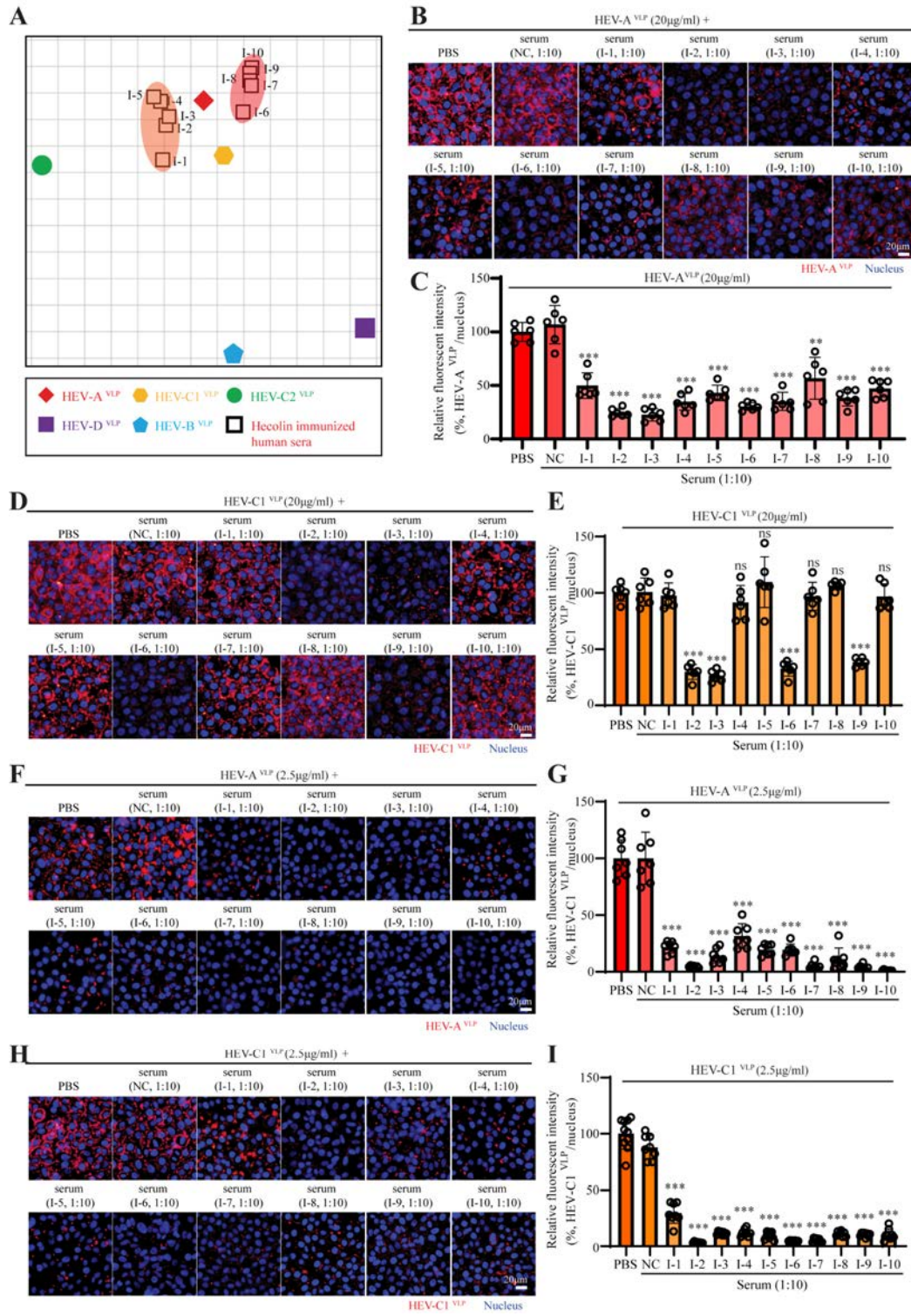ng/well of HEV-A$^{VLP}$, HEV-C1$^{VLP}$, HEV-C2$^{VLP}$, HEV-D$^{VLP}$ and HEV-B$^{VLP}$. The plates were incubated with the serially diluted serum samples. The reactivity of anti-HEV-1$^{VLP}$ IgG to five different VLPs was examined by ELISA.

34

413

414

**Fig. S26. Hecolin® immunized human sera showed partial cross-protection against the binding of HEV-C1$^{VLP}$. (A)** Two-dimensional antigenic map of HEV-A$^{VLP}$, HEV-C1$^{VLP}$, HEV-

35

C2$^{VLP}$, HEV-B$^{VLP}$ and HEV-D$^{VLP}$ with Hecolin® immunized human sera. The vertical and horizontal axes both represent antigenic distance. One unit of antigenic distance denotes a two-fold difference in sera titers. The red solid diamond, orange hexagon, green circle, purple square and blue pentagon represent HEV-A$^{VLP}$, HEV-C1$^{VLP}$, HEV-C2$^{VLP}$, HEV-B$^{VLP}$ and HEV-D$^{VLP}$ respectively, whereas the hollow squares represent serum samples collected from ten individuals immunized with Hecolin®. **(B and C)** The inhibitory efficacy of Hecolin® immunized human sera (dilution 1:10) against the binding of HEV-A$^{VLP}$ (20 μg/ml) to HepG2 cells was measured by immunofluorescence assay. The relative fluorescent intensity was quantified by ImageJ software based on three independent experiments. **(D and E)** Same as (B and C) for detecting the inhibitory efficacy of Hecolin® immunized human sera (dilution 1:10) against the binding of HEV-C1$^{VLP}$ (20 μg/ml). **(F and G)** Same as (B and C) for detecting the inhibitory efficacy of Hecolin® immunized human sera (dilution 1:10) against the binding of HEV-A$^{VLP}$ (2.5 μg/ml). **(H and I)** Same as (F and G) for detecting the inhibitory efficacy of Hecolin® immunized human sera (dilution 1:10) against the binding of HEV-C1$^{VLP}$ (2.5 μg/ml).
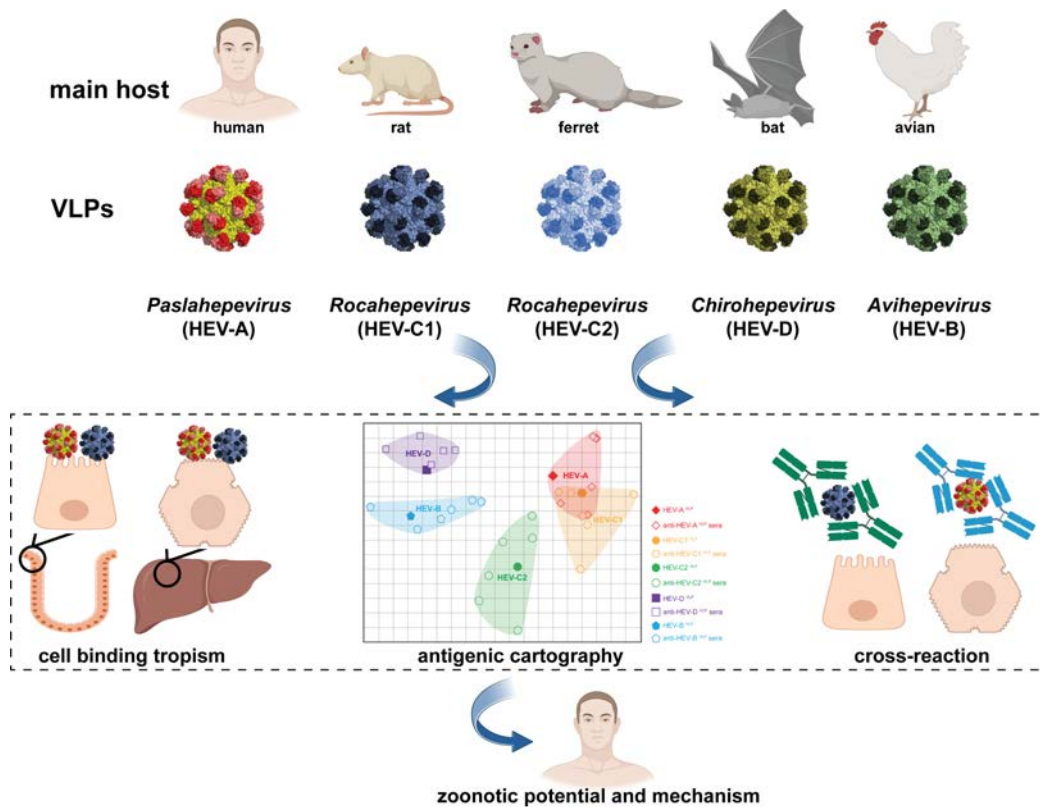
433    **Fig. S27. Graphical summary.** Cell binding tropism is a pivotal determinant of different HEV

434    species regarding their zoonotic transmission to humans. Rat HEV VLPs and infectious rat

435    HEV particles bind and enter human target cells, whereas ferret, bat and avian HEV VLPs show

436    marginal or no cell binding and entry potency. Rat HEV exhibited partial cross-reaction with

437    HEV-A, and anti-HEV-A sera partially cross-inhibited the binding of rat HEV[VLPs] to human

438    target cells. Our study revealed mechanistic insights regarding the distinct zoonotic potential of

439    different HEV species, and elucidated their cross-species antigenic relationships and serological

440    responses.

441

442    **Table S1. Amino acid sequence identity of ORF2 (HEV-A to HEV-D)**

443

| | HEV-A ORF2 | HEV-C1 ORF2 | HEV-C2 ORF2 | HEV-D ORF2 | HEV-B ORF2 |
|---|---|---|---|---|---|
| **HEV-A ORF2** | | 58 | 59 | 52 | 47 |
| **HEV-C1 ORF2** | | | 80 | 52 | 45 |
| **HEV-C2 ORF2** | | | | 53 | 46 |
| **HEV-D ORF2** | | | | | 47 |
| **HEV-B ORF2** | | | | | |

444

445

446

447    **Table S2. Amino acid sequence identity of ORF2$^T$ (HEV-A to HEV-D)**

448

| | HEV-A ORF2$^T$ | HEV-C1 ORF2$^T$ | HEV-C2 ORF2$^T$ | HEV-D ORF2$^T$ | HEV-B ORF2$^T$ |
|---|---|---|---|---|---|
| **HEV-A ORF2$^T$** | | 57 | 60 | 48 | 45 |
| **HEV-C1 ORF2$^T$** | | | 84 | 47 | 41 |
| **HEV-C2 ORF2$^T$** | | | | 49 | 44 |
| **HEV-D ORF2$^T$** | | | | | 45 |
| **HEV-B ORF2$^T$** | | | | | |

449

450    **Reference**

451

452    1.    Z. Wu *et al.*, Deciphering the bat virome catalog to better understand the ecological
453          diversity of bat viruses and the bat origin of emerging infectious diseases. *ISME J* **10**, 609-
454          620 (2016).
455    2.    D. J. Smith *et al.*, Mapping the antigenic and genetic evolution of influenza virus. *Science*
456          **305**, 371-376 (2004).
457    3.    S. Sridhar *et al.*, A small animal model of chronic hepatitis E infection using
458          immunocompromised rats. *JHEP Rep* **4**, 100546 (2022).
459    4.    H. Guo *et al.*, Drug repurposing screen identifies vidofludimus calcium and pyrazofurin as
460          novel chemical entities for the development of hepatitis E interventions. *Virol Sin*
461          10.1016/j.virs.2023.11.006 (2023).
462    5.    N. Jothikumar, T. L. Cromeans, B. H. Robertson, X. J. Meng, V. R. Hill, A broadly reactive
463          one-step real-time RT-PCR assay for rapid and sensitive detection of hepatitis E virus. *J*
464          *Virol Methods* **131**, 65-71 (2006).
465    6.    S. Sridhar *et al.*, Rat Hepatitis E Virus as Cause of Persistent Hepatitis after Liver Transplant.
466          *Emerg Infect Dis* **24**, 2241-2250 (2018).
467    7.    D. B. Smith *et al.*, Update: proposed reference sequences for subtypes of hepatitis E virus
468          (species Orthohepevirus A). *J Gen Virol* **101**, 692-698 (2020).
469    8.    D. B. Smith *et al.*, Proposed reference sequences for hepatitis E virus subtypes. *J Gen Virol*
470          **97**, 537-542 (2016).

471